NTNU
Norwegian University of
Science and Technology

Comparison of two diffusion weighted MR protocols for detecting Differences in Microvasculature in chronic Pancreatitis and Pancreas Cancer

Ingrid Boland

Master of Science in Physics and Mathematics
Submission date: July 2016
Supervisor: Pål Erik Goa, IFY

Norwegian University of Science and Technology
Department of Physics

Comparison of two Diffusion weighted MR-protocols for detecting Differences in Microvasculature in chronic Pancreatitis and Pancreas Cancer

Ingrid Boland

Trondheim, 2016

Acknowledgement

This thesis was written as a part of my master degree in applied physics and mathematics at the Norwegian University of Science and Technology, NTNU, in Trondheim. It was completed during the spring 2016 and performed in collaboration with St. Olavs Hospital.

First and foremost I would like to thank my supervisor at St. Olav Hospital Else Marie Huuse-Røneid for all help and guidance during this project. I am grateful for all the assistance and advice she has given me. Without her help I wouldn't have been able to complete my thesis.

I would also thank my supervisor at NTNU, Pål Erik Goa, for advice and guidance when needed, and the radiographers at St. Olavs Hospital, especially Inger-Johanne Rønning Dahle, for helping me with the challenges in interpretation of the images.

Last I would like to express my gratitude to St. Olavs Hospital for providing me with the time and resources necessary to conduct my study.

Abstract

Pancreatic cancer is a type of cancer with high mortality. Unspecific, or the absence of, symptoms result in late diagnosis, which is fatal when the only curable treatment is surgical removal of the tumor. Differentiating pancreatic cancer from chronic pancreatitis is especially challenging.
Studies show that the intravoxel incoherent motion-model in diffusion weighted MR imaging have promising result in differentiating pancreatic cancer from chronic pancreatitis, due to significant difference in the perfusion fraction.

At St. Olavs Hospital a traditional diffusion weighted protocol is applied as a standard protocol in the diagnosis of pancreatic cancer. Since this protocol does not differentiate between pancreatic cancer and chronic pancreatitis a new diffusion weighted protocol for detecting differences in microvasculature in chronic pancreatitis and pancreatic cancer is under development.
In this work the image quality in two imaging protocols are compared. One is a respiratory triggered protocol and the second is a free breathing protocol where a median image was calculated in order to overcome motion artifacts. These protocols were added to the standard MRI examination, in a 1.5 tesla MR-scanner at St. Olavs Hospital, in 8 patients scheduled for clinical MR of pancreas.
Images from 7 patients were used to compare image quality in the terms of ghosting, sharpness and signal-to-noise ratio. The image quality were superior in the respiratory triggered images, less ghosting, higher sharpness and a significant higher signal-to-noise ratio compared to the free breathing images. One patient with high suspicion of tumor was included at the end of the study, as a proof of method and to evaluate whether the image quality was sufficient. The simplified model relative enhanced diffusion (RED) was used in the data analysis. Based on this single patient the RED model seems promising.

Based on the work present in this thesis it was concluded that the respiratory triggered protocol, due to the highest image quality, should be the base for further development of a new diffusion weighted protocol for pancreas. With the quality of the respiratory triggered images the RED model is promising and should be subject for further investigation.

Sammendrag

Pankreaskreft er en kreftform med høy dødelighet. Ingen eller lite spesifikke symptomer fører til sen diagnose noe som er fatalt da kirurgisk fjerning av tumor er eneste kurative behandling. Særlig vanskelig er det å skille pankreas kreft fra kronisk pankreatitt.
Studier viser at intravoxel incoherent motion-modellen i diffusjonsvektet MR avbildning gir lovende resultater for differensiering av pankreas kreft og kronisk pankreatitt, med signifikant forskjell i perfusjons fraksjonen.

Ved St. Olavs hospital benyttes en tradisjonell diffusjonsvektet sekvens som standard protokolle ved diagnostisering av pankreaskreft. Da denne protokollen ikke skiller pankreaskreft fra kronisk pankreatitt arbeides det nå med å utvikle en ny diffusjonsvekted protokoll for deteksjon av mikrovaskulære ulikheter i pankreaskreft og kronisk pankreatitt.

I dette arbeidet sammenliknes bildekvaliteten i to ulike avbildingsprotokoller. Den ene er en respirasjons trigget protokol mens den andre er en fri pust protokoll. Disse protokollen ble lagt til den standard MR-undersøkelsen, på en 1.5 tesla MR-scanner ved St. Olavs Hospital, hos 8 pasienter som var henvist til MR av pankreas.
Bildene fra 7 pasienter ble benyttet i sammenlikning av bildekvalitet, i form av bildeskarphet, ghosthing og signal-støy forhold. Bildeikvaliteten viste seg å være best i de respirasjonstriggede bildene, med høyere bildeskarphet, mindre ghosting og signifikant bedre signal-støy forhold sammenliknet med fri pust bildene. Mot slutten av arbeidet ble en pasient med høy mistanke om tumor inkludert som et bevis på metoden og for å vurdere om tilstrekkelig bildekvalitet er oppnådd. Den forenklede modellen relative enhanced diffusion (RED) ble brukt til dataanalyse. Basert på resultatet i denne ene pasienten ser RED modellen lovende ut.

Basert på arbeidet i denne oppgaven ble det konkludert med at den respirasjonstriggede protokollen, på grunnlag av høyest bildekvaliet, burde bli benyttet for videre utvikling av ny diffusjonsvektet protokoll for pankreas. For bildekvalitet tilsvarende den i de respirasjonstriggede bildene virker RED som en lovende modell, og bør derfor utforskes videre.

Abbreviations and Nomenclature

Abbreviation and nomenclature used throughout the thesis.

Abbreviation	Meaning
ADC	Apparent Diffusion Coefficient
b	Degree of diffusion weighting
D	Diffusion Coefficient
D*	Pseudodiffusion Coefficient
DWI	Diffusion Weighted Images
EPI	Echo Planar Imagning
f_p	perfusion fraction
G_{diff}	Diffusion Gradient
G_{PE}	Phase Encoding Gradient
G_{SS}	Slice Selection Gradient
G_{RO}	Read Out Gradient
GRAPPA	Generalized Autoclibrating Particular Parallel Acquisition
IVIM	Intravoxel Incoherent Motion
NET	Neuroendocrine Tumor
PDAC	Pancreatic Ductal Adenocarcinoma
PE	Phase Encoding
RED	Relative Enhanced Diffusivity
RF	Radio frequency
RO	Read Out
ROI	Region of Interest
SNR	Signal-to-Noise ratio

LIST OF FIGURES

LIST OF TABLES

CONTENTS

CHAPTER 1

INTRODUCTION

1.1 Pancreas

The pancreas is the largest digestive gland and performs a range of vital exocrine and endocrine functions. The functions are complex but they can be summarised as the contribution to digestion and regulation of the blood glucose level. This is achieved by secretion of pancreatic juice with enzymes to the duodenum and secretion of hormones into the blood stream [1].

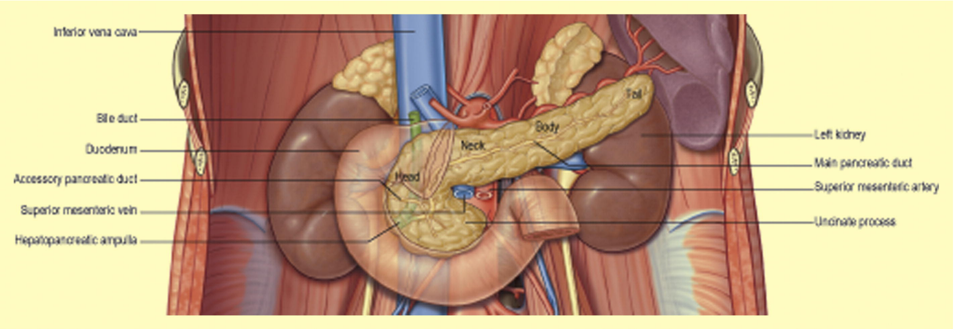

Figure 1.1: An illustration of the pancreas, displaying the different segments and the location of the organ [2]

The pancreas it located in the abdominal cavity at the transpyloric plane, the level of the first lumbar vertebrae. The organ is divided into four segments; head, neck, body and tail as illustrated in Figure 1.1. The head is located in the C-curve of the duodenum, extending into the neck, body and ending in the tail that is bordering the spleen. Macroscopically the pancreas i lobulated and is contained with a fine fibrous network and the main duct running throughout the length of the pancreas. The main duct is commonly joined with the termination of the common bile duct before it enters the duodenum. Thus secreting both pancreatic juice and bile from the liver and gall bladder simultaneously. In addition to the main duct an accessory pancreatic duct also secrete pancreatic juice into the duodenum, through an opening about 2 cm above the main duct. The location, size, and anatomy can vary among individuals [2].

1.1.1 Pancreatic cancer

Pancreatic cancer is one of the most deadly forms of cancer, with an estimated total 5 year survival of 5.5% for male and 6.8% for female in Norway in 2010-2014. Thus being the cancer type that takes fourth most lives in both women and man even though it is a relatively rare type of cancer, responsible for 2.3% of all cancer diagnosis [3]. The poor prognosis is a result of the disease responding poorly to radiation and chemotherapy in addition to unspecific, or the absence of, clinical signs, causing diagnosis often to be set in the later stages of the cancer development [4]. The cancer has often spread throughout the pancreas, or even further, making it inoperable. Though when diagnosed early and the tumor can be removed surgically the prognosis improve radically, the 5 year survival for localised pancreatic cancer is estimated to 23.2% for male and 21.7% for female in Norway 2010-2014 [3]. Hence a desperate need for diagnostic tools that helps an earlier diagnosis.

The clinical most important differential diagnosis to pancreatic cancer is chronic pancreatitis. Chronic pancreatitis is chronic inflammation in the pancreas, occurring when the digestive enzymes of the pancreatic juice activating inside the pancreas starting to degrade the pancreatic tissue resulting in a damaged pancreas with irreversible impairment to both endocrine and exocrine function [1]. Chronic pancreatitis can display the same symptoms as pancreatic cancer and form benign masses. Additionally pancreatitis can mimic pancreatic cancer in dynamic CT and MR imaging making preoperative distinction difficult [5].

1.2 MRI

This section contains an introduction to the theory behind magnetic resonance imaging needed to understand the content of this thesis. The theory is only superficial, however for a more extensive description of theory behind the physics of MR imaging; Magnetic Resonanance Imaging by E. M. Haacke can be recommended.

Magnetic resonance imaging, MRI, is an imaging technique that is widely applied clinically in soft tissue imaging, in determining if tissue is pathological as well as in study of anatomical structures. Since it, in contrast to most imaging techniques, doesn't depend on ionising radiation it is a safe imaging method that if applied correctly doesn't cause any harm, or an increased cancer risk, to the patient.

In MRI the interaction between a magnetic field and the quantum mechanical spin properties of the nucleus is utilised. Nucleus with spin can be considered to rotate around an axis

at a constant velocity thus creating a magnetic momentum. Most elements have isotopes that posses spin, but in clinical MRI ^{1}H is the isotope utilised. ^{1}H is the most abundant isotope of hydrogen which is a main component of both fat and water, hence being abundant in all soft tissues in the body [6].
When nuclei with spin are placed in a strong external magnetic field the nuclei will align so that the magnetic momentum of the nucleus will be parallel or antiparallel with the magnetic field with the Boltzmann distribution

$$\frac{n_\uparrow}{n_\downarrow} = e^{\Delta E/kT}. \tag{1.1}$$

Where $n_\uparrow$ represent the amount aligned parallel to the magnetic field and $\mathrm{n}_\downarrow$ anti parallel, k is the Boltzmann constant, T is the absolute temperature and $\Delta\mathrm{E}$ is the energy difference between the two states. For ^{1}H at 1.5T in a human body only a small majority is aligned parallel to the magnetic field ($\sim 10^{-6}$)[6].

However the spins are not stationary, they process around the axis of the magnetic field. This precession is out of phase but with the same frequency, defined as the Lamour frequency

$$\omega = \gamma B_0. \tag{1.2}$$

Where γ is the gyromagnetic ratio, a property of the nucleus, and B_0 is the strength of the magnetic field in tesla. Hence the precision rate is proportional to the magnetic field strength. The phase differences result in a cancelling of the transverse component and the sum of the magnetic momentum result in a magnetisation vector in the direction of the magnetic field. The subsequent application of a radio frequency pulse, RF pulse, excites the spin and move them into phase. Thus flipping the magnetisation vector, with an angle depending on the amplitude and duration of the RF pulse, creating a transverse component of the magnetisation vector [7]. The magnetisation vector is still rotating with a constant velocity, creating an electric current, the signal, that can be picked up by receiver coils which are placed on the patient [8].

After application of a RF pulse the magnetisation returns to its original state, a process called the relaxation. There are two types of relaxation, the transverse and the longitudinal. The longitudinal relaxation is due to energy exchange with the environment, the protons release the energy absorbed from the RF pulse. The time from the RF pulse to the magnetisation vector reaches 63% of its original state is defined as the T1. Therefore it is also called the T1 relaxation.
The transverse relaxation is an effect of exchange of energy between adjacent spins causing them to dephase. Eventually the spins end up cancelling each other and the transverse component of the magnetisation vector is lost. The time from RF pulse to the transverse magnetisation has decayed to 37 % of its maximum value is defined as the T2, thus the relaxation is also called the T2 relaxation [7]. In Figure 1.2 the transverse and the longitudinal relaxation process are shown.

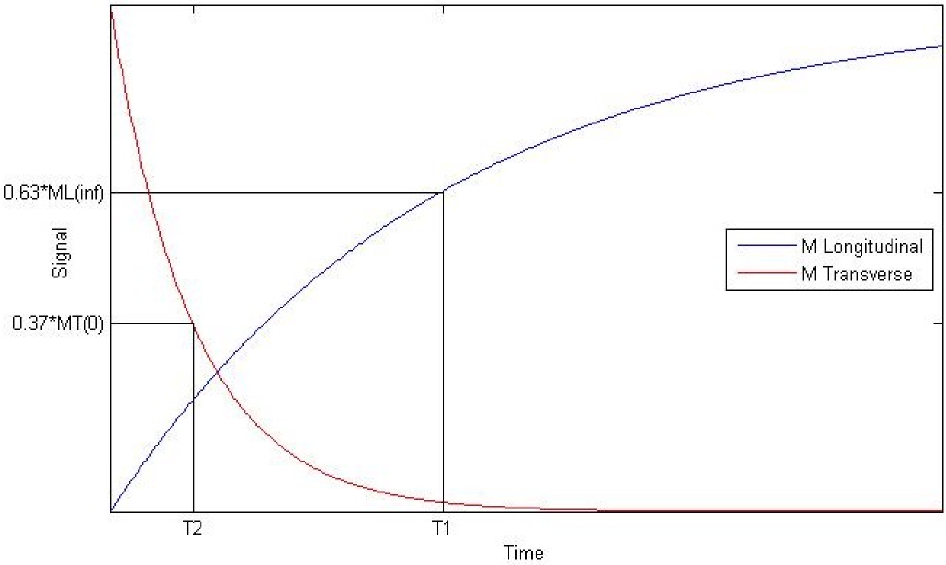

Figure 1.2: A illustration of the longitudinal-, in blue, and the transverse, in red, relaxation of the signal in a MRI process where the RF pulse is turned off at time t=0. The relaxation times T_2 and T_1 and their corresponding values in signal are marked in the illustration.

Gradients and repetition of RF pulses have been combined in different orders and magnitudes in order to create different sequences. The objectives of the different sequences can vary from enhancing a specific property within the anatomy, or generating images faster. Spin echo and gradient echo are sequences that many clinically applied sequences are based on. In spin echo a second RF pulse is applied in order to reverse the dephasing of the spins; rephasing. Resulting in an echo of signal. The echo time, TE, is the time it takes from the RF pulse to the signal induced in coil peaks again. A MR sequence is often repeated several times during a scan, the time between two repetitions are called the repetition time, TR [7].
In a MR sequence the TR and TE can be altered and combined in different manners in order to weight different properties of anatomical structure. T1- and T2 weighting are the most common. A T1 weighted image is obtained with short TR and TE, resulting in an image where the fluid is dark while the fat is bright, in contrast a T2 weighted image is obtained with a long TE and TR, and in the resulting image the fluid is bright and the fat is intermediate bright [7].

1.2.1 Image Formation

In order to use the recorded signal to create images the signal must be incorporated with some sort of spatial encoding. Application of magnetic gradient in three orthogonal directions are utilised in order accomplish this. The applications of a magnetic gradient changes the effective magnetic field along the direction of the gradient as described in equation:

$$B_{eff} = B_0 + G \cdot z, \tag{1.3}$$

where B_{eff} is the magnetic field at position z. As known the spins precess with a frequency proportional to the magnetic field, hence the the spins in a magnetic gradient will rotate with spatial dependent frequencies during the gradient, and at the end of the gradient a spatial dependent phase shift has been established.

The initial step in spatial encoding is the slice selection. Here a slice selection gradient, G_{SS}, is applied simultaneously as the RF-pulse. Hence only one slice have spins rotating with the resonance frequency of the RF-pulse and will be excited by the RF-pulse and subsequent be the origin to the detected signal. The orientation of the slice is determined by the direction of G_{SS} and the thickness is determined by the bandwidth of the RF pulse [6]. The first dimension within the selected slice is encoded for by a gradient called the phase encoding gradient, G_{PE}. A gradient applied in between the RF pulse and the signal read out. This gradient encode the slice with a one dimensional spatial dependent phase differences. The second dimension within the slice is encoded by a gradient applied simultaneously as read out of the signal, the read out gradient, G_{RO}. This gradient give frequency encoding, the recorded signal have an one dimensional spatial dependent frequency difference. [6].
This process is repeated several times with different magnitudes to G_{PE}, resulting in different dephasing in each repetition [6]. The different gradients and the order of application is shown in Figure 1.3.

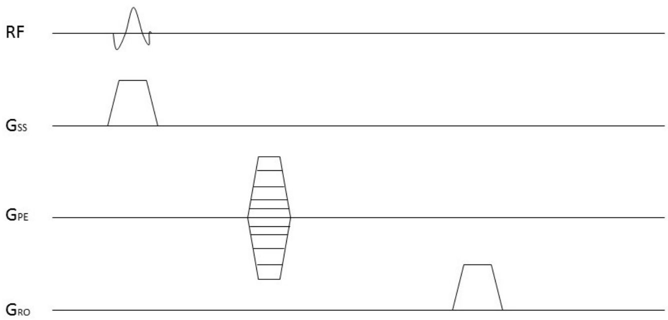

Figure 1.3: A sequence diagram of the RF pulse and the gradients, G_{SS}, G_{PE} and G_{RO}, applied in order to get spatial encoding in a MR-signal hence being able to create an image.

K-Space

The recorded signal is saved in a graphic 2D matrix called the k-space. In the k-space the data are displayed in the time domain, thus all the point in the k-space contain information from all position within the slice. By performing a 2D Fourier transformation of the k-space the data is transformed into the frequency and phase domain, since these properties are spatially dependent the result of a 2D Fourier transform is an image where signal magnitude is represented in order to its spatial location [6].

1.2.2 Echo Planar Imaging

One of the most important criteria in MRI sequences is the time consumption. The probability of bulk motion and the amount of motion is proportional to the time span. Clinically it is also important maximise the number of patient within the time available. Therefor ultra-fast sequences have been developed. Echo Planar Imaging, EPI, was the first of these sequences, but due to limitations within the hardware available it was first implemented clinically in the 1990's [9].

In a EPI a long gradient train is applied after the RF pulse in order to fill a larger part of the k-space within one repetition. In an single shot EPI sequence the whole k-space is filled in one RF pulse while in multishot EPI several repetitions are required in order to fill k-space [9]. In Figure 1.4 a common EPI pulse sequence and k-space filling is illustrated. The sequence start with the excitation by an RF pulse and G$_{SS}$ simultaneously. Followed by the application of negative G$_{PE}$ and G$_{RO}$ which positions at the negative extremes in both phase and read directions in k-space. Afterwards a gradient train is applied in read out direction, the gradient train is a continuous line of gradients, all with the same magnitude but with altering polarity. Polarity decides the way it fills k-space, negative move in right direction while positive moves in left directions. When the polarity switch, a small G$_{PE}$ of positive polarity, a gradient blip, is applied; this moves up in the k-space, in positive phase direction [8].

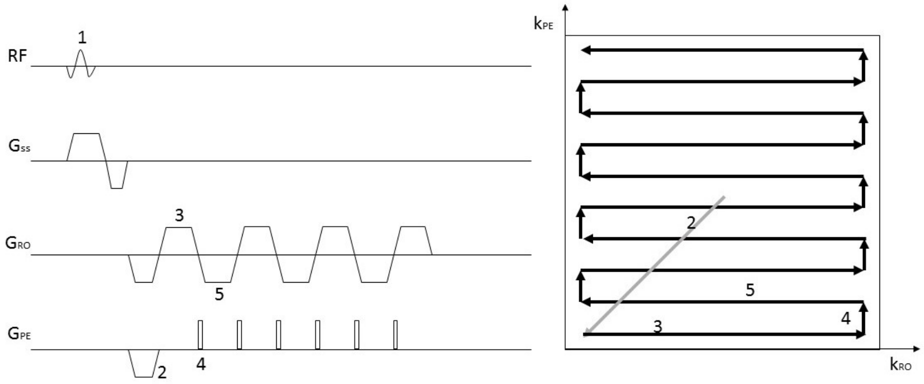

Figure 1.4: Illustration of the EPI gradient sequence with subsequent k-space filling. (1) A RF pulse is applied in order to cause the initial dephasing, (2) gradient are applied moving into the negative extremes of both phase and read direction of k-space, (3) the gradient train starts with a positive G_{RO} encoding a line in positive read direction in k-space, (4) A blip of a G_{PE} moves the k-space position up a line before (5) a negative G_{RO}, the next in the gradient train, encodes the next line in k-space in negative direction. The application of blip G_{PE} between G_{RO} of altering polarity continues until the whole, or a larger part of, k-space is filled.

In other versions of EPI the application of G_{PE} and G_{RO} is changed and thereby also the pattern of filling in k-space. An example is the continuously application of constant G_{PE}, instead of the blip in the version above, resulting in zig-zag pattern in k-space [10].

1.2.3 GRAPPA - Generalized Autocalibrating Particular Parallel Acquisition

Multicoiled arrays are often applied in order to detect the signal. In Generalized Autocalibrating Particular Parallel Acquisition (GRAPPA) the different sensitivity and location of the coils is used in signal processing to generate spatial information that otherwise would be obtained by applying gradients. Thus decreasing number of required lines in k-space and scanning time. For instance an acceleration factor of 2 reduce the number of acquisitions to the half. However less signal is put into k-space resulting in a lower SNR. Additionally the ability to measure the exact sensitivity of the coils and movement of coil between coil calibration and images acquisition is limiting factors [11].

1.3 Imaging Artifacts

MR images often contain artifacts, intensities in the images that do not correspond to the actual features in the object studied. Such as features recorded in the wrong place or in the right place but with wrong intensity or bogus in the image with no relation to the real sample. Artifacts can originate from the instrumentation, the experimental design or the sample itself [8]. In order to get the correct diagnosis its important to understand, and if possible correct, artifacts. Some artifacts are easy to identify as artifacts while others are not and just give false information to the image. Some sequences, such as EPI, are more prone to artifacts then others [7].

1.3.1 Motion Artifacts

Bulk motion to the patient cause great artifacts in MR images. The spatial encoding no longer corresponds to a constant anatomical locations and the origin of a position in the image is several different positions in the anatomy. Hence a structure might appear several times or not at all, this degrade the image quality. Additionally the slices can appear as unconnected. Bulk motion can come from voluntary motion of the patient. Patient often move to release pain and discomfort or have muscle cramps if the position in the scanner is uncomfortable [10].

In addition the body is subject to a range of vital involuntary and voluntary motions of organs. Such as peristalsis, cardiac- and respiratory motion. Peristalsis is the wavelike contraction of the smooth muscle layer in the digestive tract pushing food from the oral to the anal end [1]. In upper abdomen peristalsis and respiratory motion is present.

Ghosting

When motion is periodic, repeated, such as blood flow and respiration the image is distorted in the phase encoding direction. The signal migth smear out in the image, resulting in a blurry image, or several less clear structures located a bit from actual structures location appear. This effect is called ghosting, due to the ghost like appearance. This is particularly a problem when high signal tissues are set in motion [8]. Ghosting occurs due to varying location of the anatomy at the application of different G$_{PE}$, in addition displacement take place between application of G$_{PE}$ and signal read out [7].

The degree of the distortion to the image by ghosting can be assessed quantitatively by the percent-signal ghosting test, developed by the American College of Radiology, ACR [12]. In this test the ghosting is reported as a percentage of the signal in the true, primary image. The ghosting ratio is determined by the equation:

$$ghostingratio = \frac{(top + bottom) - (left + right)}{2 \cdot ROI} \tag{1.4}$$

where top, bottom, left and right is the mean signal of regions within the placement described in reference to the body of a phantom, and ROI is a large region within the phantom. Thus the background is removed and the ratio is the signal due to ghosting divided by the true signal. This test is applied to phantoms in quality control of the MR scanner and the ghosting ratio should be less than or equal to 0.025 = 2.5%. Otherwise it can indicate hardware problems [12].

1.3.2 Motion Artifact Remedies

In order to prevent and correct for motion artifacts several methods can be applied. Making the patient comfortable and calm, immobilising with straps and pads, and explaining the

patient the importance of keeping still are actions that are applied in order to prevent voluntary motion. Additionally the scan time is always kept at a minimum, in order to minimise the probability of movement [7].
In additions several motion limitation strategies and motion correction can be applied:

Antiperistaltic Drugs

Peristaltic motion is a part of the digestion and is enhanced by eating. The patients can meet fasting in order to reduce peristalsis. T. Hillestad in found fasting to not reduce peristaltic motion sufficient to get adequate image quality in DWI of pancreas [13].
Alternatively th intestine can be anaesthetised by the administration of Buscopan (hyoscine butylbromide). Buscopan is an antiperistalic drug that freezes the peristaltic motion for 15-20 minutes [10]. At St.Olav administration of Buscopan has for a long period been standard procedure in DWI of the lower abdomen and January 2016 it was also included in the standard DWI protocol for the upper abdomen, where pancreas is located. Although Buscopan might cause the patient discomfort through side effects such as dry mouth, blurry vision and dizziness [14].

Breathing techniques

In order to circumvent respiratory motion different breathing techniques can be applied, such as breath holding and respiratory triggering.

In breath hold imaging the patients holds its breath while the imaging is conducted. In order to get good images it is important that the patients holds the same volume of the lungs through out the entire scan. The breath hold can be repeated several times, in order to get several slices, but same volume have to be obtained in all repetitions in order to get required image quality, this has proven difficult. Hence it is preferable to get the entire imaging within one breath hold, which gives an extreme time limit with the entire scanning to be conducted in under 25 seconds [10].

In respiratory triggered imaging the idea is that the imaging is conducted within a limited range of the respiratory cycle, thus limiting the motion range. This is accomplished by placing a navigator echo in the chest tracking the diaphragmatic motion. The navigator echo communicates with the scanner ensuring that imaging is conducted in the same phase of the respiratory cycle throughout the entire scanning. This is often in the exhalation phase of the respiratory cycle.
The limitation of the range of motion reduces the motion artifacts. The drawback is that the scanning is time consuming since the imaging can only be repeated each respiratory cycle. With a normal breathing pattern TR is at least 4000 ms. This could be dramatically increased if the patients breaths slowly. Additionally if the breathing is irregular the image quality is distorted, and might end up being worse than if no motion correction was preformed. Hence the quality of the images might vary, depending on the patient [10].
Kartalis et. al. suggested that on patient with pancreatic cancer the respiratory triggering

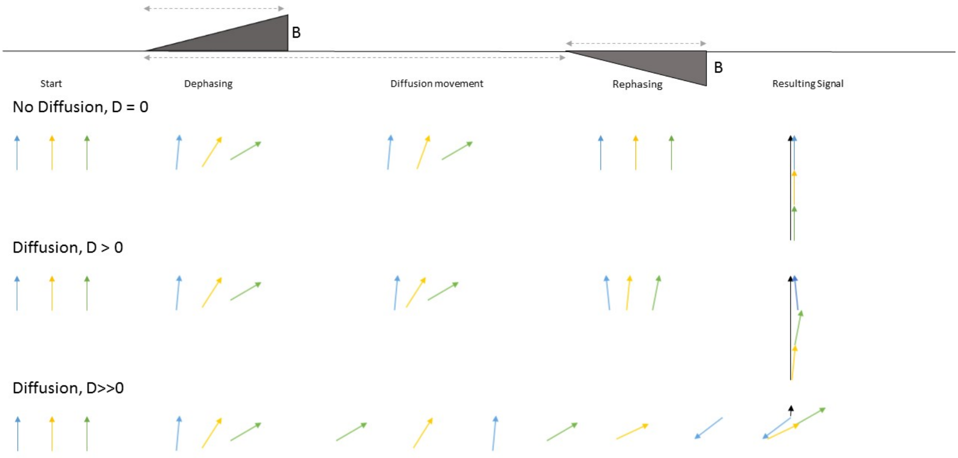

Figure 1.5: Illustration of how spins without diffusion, low diffusion and high diffusion is affected in a DW-MRI sequence, and how the diffusion affect the resulting signal.

were superior to the other breathing methods, including breath hold and free breathing [15].

Averaging

By acquiring several repetitions and then averaging the recorded signal voxelwise, each voxel will contain the mean value of the signal recorded over time in that explicit voxel. Signal originating from motion is more random in nature then the actual signal, thus the signal caused by motion will to some degree be averaged out and be less present in the final image [7]. This technique will also minimise the background noise.
Creating a median image is an alternative to averaging. In a median image each voxel is filled with the median voxel values, thus extreme values at either end does not affect the resulting voxel value.

1.4 Diffusion-weighted MRI

Diffusion is random motion of particles caused by thermal energy [9]. If the diffusion is isotropic the particles move an arbitrary length in an arbitrary direction, if the particles are restricted in some direction the diffusion is anisotropic [6].

In MRI magnetic gradients are applied to induce phase shift between nuclei, and thus creating different phases in an ascending order depending on spatial location. Diffusion of protons move these proton out of ascending order. In Figure 1.5 the behaviour of spins and their resulting signal in DWI is illustrated, both when diffusion is present and absent. In DWI two strong gradients, G_{diff}, are applied. The first gradient is applied to cause

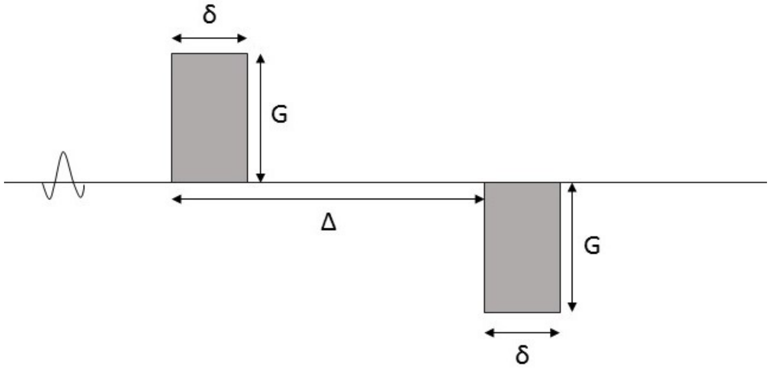

Figure 1.6: Illustration of the Gradient sequences, G$_{diff}$ in Diffusion weighted imaging, with the different properties of the sequence indicated.

dephasing depending on position and the second gradient is applied to cause rephasing. Movement due to diffusion gives a difference between the two gradient strength experienced by an individual nucleus, and the rephasing will be partly unsuccessful depending on the degree of diffusion. Hence the nucleus will still be out of phase after the second gradient. This will result in a loss of signal and the signal will depend on the degree of diffusion in manner described by equation

$$S(b) = S(0)e^{-D}, \tag{1.5}$$

where D is the diffusion coefficient, , S(0) is the signal when there is no diffusion weighting and b is the b-value, a value representing the degree of diffusion weighting in [16]. The b-value is defined as

$$b^2 = \gamma^2 G^2 \delta^2 (\Delta - \delta/3), \tag{1.6}$$

where γ is the gyromagnetic ratio, G is the gradient strength, δ is the duration of the gradient and Δ is the diffusion time, the time between the two gradients. In Figure 1.6 the gradient sequence that causes diffusion weighting is illustrated. From the illustration it is clear to see that the $G^2\delta^2$ is the square of the area of the gradient. Figure 1.6 also shows that the b-value can be altered by changing the gradient strength, duration, time between or number of gradients. Or a combination of several of the aforementioned [10].

Equation 1.5 assumes a free diffusion. However in tissue this assumption is not necessarily true and the measured signal is affected by other processes than only the pure diffusion, hence in DW-MRI the detected diffusion coefficient is instead called the apparent diffusion coefficient, ADC. Acquisition with at least two different b-values is applied to deduce ADC values through the relationship

$$ADC = \frac{1}{b_1 - b_2} ln\left(\frac{S(b_1)}{S(b_2)}\right). \tag{1.7}$$

Thus being able to create an ADC map, an image of ADCs in their spatial location [16]. The diffusion differ between tissues depending on the tissue structure. In pathological tissue the structure, and the diffusion, is often altered. Tumours frequently are more cellular than the healthy tissues they originate from. The diffusion is inversely proportional to the cellularity, hence tumors often have a relatively high signal in DWI [17].

1.4.1 IntraVoxel Incoherent Motion

In biological tissue perfusion can mimic diffusion. The capillaries might be orientated in a quasi-random way, resulting in a flow through the capillaries that in MRI is indistinguishable from tissue diffusion. This effect is called intravoxel incoherent motion (IVIM) [18]. Hence a more correct signals diffusion dependence is described when a voxel is assessed to contain two compartments, one compartment within the capillaries and one compartment outside the capillaries. The compartments will experience different apparent diffusion, the pseudodiffusion in capillary compartment and tissue diffusion in the compartment outside the capillaries. Summation of the signal from the two compartments result in the biexponential equation

$$S(b) = S(0)(f_p e^{-bD^*} + (1 - f_p)e^{-bD_t}). \tag{1.8}$$

where D^* is the pseudodiffusion coefficient, D_t is the diffusion coefficient and f_p is the blood volume fraction. With application of this equation instead of monoexponetial equation the diffusion can be separated from the pseudodiffusion, and then ten enable creation of maps of both D^*, D_t and f_p. All parameters in the IVIM model can be altered in pathological tissue, and multiple parameters might help differentiate between different diseases [18].

Diffusion is a very fast process within the nanometre range while pseudodiffusion is comparatively much slower process, in the range of tens of micrometres. Thus the pseudodiffusion contribute to ADC for b-values in the low range, $0<b<200$ [s/mm^2], depending on the velocity of the flow, slow velocity contribute in higher b-values than a high velocity [18].

1.4.2 Relative Enhanced Diffusivity

In clinical imaging there is always several considerations, image quality and duration of the scan is often opposing components. In high quality IVIM imaging A. Lemke et. al. concluded that at least 10 b-values should be applied, preferably more, in order to get a satisfying quality [19]. This would result in a time consuming scanning protocol. In clinical application time span is important, probability of bulk motion increases with scanning time and cost increases due to longer examination times.

As an alternative the Relative Enhanced Diffusivity (RED) imaging method was recently developed at St. Olavs Hospital and NTNU by J. Teurel et. al.[20]. The RED imaging is a technique that is in agreement with IVIM but it does not differentiate between perfusion and diffusion [20]. In RED imaging of only 3 different b-values are necessary, these are utilised in order to create two ADC maps. The b-values are set to be in the ranges of low and medium diffusion weighing, example b-values of 0, 200, and 800, resulting in one

ADC map where perfusion is profound, ADC$_{low}$, and one where the perfusion is virtually absent, ADC$_{medium}$ [20]. These ADC maps are then used to create a RED map with RED values created with equation:

$$RED = 100 \cdot \left(\frac{ADC_{low} - ADC_{medium}}{ADC_{medium}}\right). \tag{1.9}$$

Thus the RED map is an image where the perfusion-diffusion ratio are displayed in respect to its spatial location in the anatomy. Thus being a method displaying changes in perfusion and diffusion while requiring a less time consuming imaging then the IVIM model, due to the only demanding three b-values. The resulting RED map can be employed in evaluating if tissue is normal or pathological. However since the anatomical information is mostly lost the RED map, or a part of a RED map, should be merged with another image where the anatomy is clearly displayed in order to identify pathological tissue.

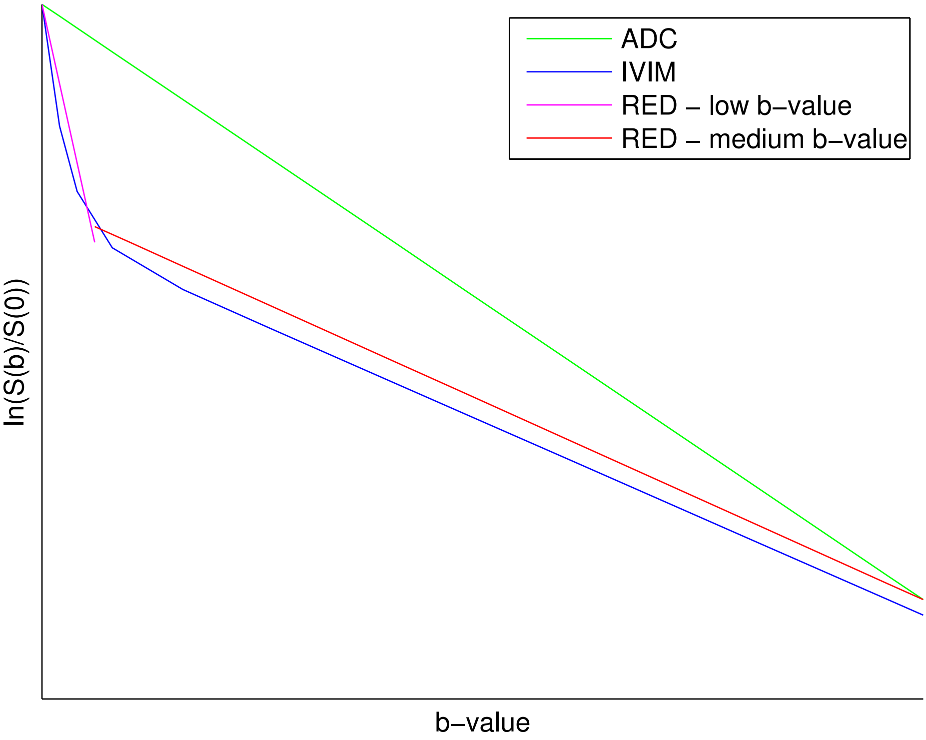

Figure 1.7: Plot of how the signal within a DW-MRI with respect to the diffusion weighting, b-values, with the different models, IVIM, RED and the traditional monoexponential equation. The plot is only created in order to illustrate the difference and similarities among the different models.

In Figure 1.7 the signal as a function of b-value is plotted for the traditional monoexponential equation, ADC, the biexponentional equation, IVIM and the two traditional monoexponential combined in order to create the RED. In the figure it is clear to see that when combining two different traditional signals, where contribution from pseudodiffusion is vastly different, the signal mimics the signal in the IVIM model. Thus even though RED can be considered a simplification that provides some of the same information as the IVIM model.

IVIM imaging of the Pancreas

Pancreatic ductal adenocarcinoma, PDAC, is the most common type of pancreatic cancer, 85-90 % of tumors in the exocrine tissue are PDAC. Other rare form of cancer in exocrine tissue can be the case, but these often have a better prognosis. Neuroendocrine tumors, NET, can occur in the pancreas, but it is uncommon and due to a distinct biological and clinical characteristics these must be held separate [21].
PDACs tend to be hypovascular due to malignant cell infiltration in the abundant desmoplastic stromas, as well as decreased vascularity. Thus PDACs have lower f_p than healthy pancreatic tissue [22] [23]. This spreads to a traditional ADC value, Klauss and Lemke found a significant lower ADC value for b values 50, 75, 100, 200 and 300, but no significant difference for b-values 25, 400 and 600, in addition to the overall ADC values [4]. The contribution from perfusion is more profound in 0<b<200, thus a reduction in perfusion would mostly affect ADC values calculated from b-values in this range.
The f_p has also been shown to be significantly higher in benign masses in chronic pancreatitis than in pancreatic cancer [4] [24] [25], although acute pancreatitis did not have the same difference [22]. Klauss and Lemke concluded that f_p was the superior DWI-derived parameter in separating chronic pancreatitis from pancreatic cancer [4].

1.5 Image Quality

Image quality is not a single factor, but the net sum of at least five factors: contrast, sharpness, noise, artifacts and distortion [26]. Imaging artifacts, focusing on motion artifacts, are described in section 1.3.

1.5.1 Signal to Noise Ratio

All medical images contain some noise, the noise is random in nature and the presence of noise gives an image a grainy appearance. Although noise give the images undesirable appearance, the main problem is that the noise can cover and reduce the visibility of some features in the images [26]. One important method to assess the level of noise in an image is the signal to noise ratio, SNR. SNR is the ratio between the real signal and the signal due to noise, calculated by

$$SNR = \frac{\mu}{\sigma} \tag{1.10}$$

where μ is the mean of the signal and σ is the standard deviation of the noise [27].
In MRI there is always a trade-off between the final SNR and other user-specified param-

eters such as resolution, scan time, field of view (FOV), and bandwidth of RF pulse. The SNR is proportional to the square root of the signal averages, thus a doubling of acquisition, and scan time, will increase the SNR in an average image with $\sqrt{2}$ [27].

1.5.2 Sharpness

The sharpness is an important factor of the image quality since it determine the amount of detail the imaging system can reproduce. The sharpness is defined by the boundaries between different zones containing different values. If the transition is sharp steps or gradual and blurry [28]. The anatomical structures vary in size, if the sharpness is low sharpness small anatomical structures will not be visible in the image [26].

The sharpness can be assessed by looking at the slope of the transitions between two zones in the image. The steeper the slope the sharper the image [28].

CHAPTER 2

AIMS

Application of IVIM model to DWI of pancreas has the potential of improving diagnosis of pancreatic cancer, assuming high quality images can be obtained. However the pancreas is subject to peristaltic and respiratory motion, thus obtaining high quality images is challenging.

The aim of this study is to compare two protocols, that are applied after administration of Buscopan, in terms of image quality. Then evaluate the benefits and drawbacks of each protocol in order to make a recommendation of which protocol the further development of a protocol should be based on. As a proof of method the relative enhanced diffusion (RED) values were created for one patient in order to see if the image quality of the protocols could give a distinguishable tumor in pancreas.

CHAPTER 3

MATERIAL AND METHODS

3.1 Study Population

The study population were patients that where scheduled for MRI of pancreas in a small period in the beginning of mars 2016. No selection was made, hence the patients physical state differed; making them good representation of the patient group that the imaging protocol is developed for. 7 patient were included in the main part of the thesis, both female and male were represented. The mean age was 68.4 ± 7.9 years.
At a late stage in the project a patient with high probability of having pancreatic cancer was included, thus being patient 8. This patient was not to be included in the post processing of the data, only as a proof of method. To evaluate if calculation of RED is a method that helps identify a tumor. Patient 8 had tumor suspicious tissue located in the head of the pancreas.

3.2 MR Imaging

All examinations were performed on the same 1.5 Tesla clinical MR-scanner (Magnetom Avanto , Siemens, Erlagen, Germany) at St. Olavs Hospital.

3.2.1 MR Protocol

Two different DWI protocols were applied on the patients as a part of this project. One with free breathing and one with respiratory triggered imaging. The protocols were not created to be equal in all aspects other than breathing method, but rather created as two protocols that would be applicable in the clinic. Both protocols were single shot EPI sequences, and GRAPPA with an acceleration factor 2 was applied in order to minimise the scanning time.

The images were obtained on patients during a the scheduled MRI examination of pancreas, thus the imaging protocol were conducted together with several other protocols, those conducted during a normal clinical scanning of pancreas. Buscopan were administrated immediately before DWI and the two sequences were run straight afterwards each other.

Table 3.1: The properties of the free breathing and respiratory triggered protocols.

	Respiratory Triggered	Free Breathing
TR	1900 ms	4200 ms
TE	68 ms	75 ms
FOV	400 mm	400 mm
Matrix	148x148	148x148
Phasedirection	AP	AP
Bandwidth	2252 Hz/Px	2598 Hz/Px
Number of slices	34	36
Voxel size	2.7 x 2.7 x 4.0 mm^3	2.7 x 2.7 x 4.0 mm^3
Diffusion directions	3	6
Averages	4	4
EPI factor	148	148
Accel. factor	2	2

Respiratory Triggered Imaging

The standard clinical DWI protocol at St. Olavs Hospital is a respiratory triggered protocol with four b-values, 0, 50, 400 and 800, that are all included in the creation of an ADC map. In order to get the experiment included in within the timescale of a normal patient procedure, and with as little fuzz as possible, another b-value, 200, was added to the standard protocol, other wise the protocol remained unchanged. The images with interesting b-values then to be extracted in post-processing. The properties of the protocol is listed in Table 3.1 and a more complete description of the protocol are added in Appendix A.2.

In patient 8 the respiratory triggered protocol were altered to include 36 slices, instead of 34 slices. Otherwise the protocol remained the same.

Free Breathing Imaging

The free breathing protocol was added only for this purpose. The properties of the sequence are listed in Table 3.1 and complete description of the protocol is in Appendix A.3. The protocol is further developed from T. Hillestads work on her master thesis [13]. The great advantage of the free breathing as oppose to any other breathing techniques is that it takes short time, as a result 6 directions were included in the protocol, twice the amount of directions in the respiratory triggered protocol. With the assumption that diffusion is isotropic addition of directions is an other way of increasing number of repetitions. Not being dependent on the navigator of the respiratory triggering there is less software limitations giving a possibility to store all images, not only average images.

3.3 Median images

The images acquired with free breathing were processed in MatLab(Mathworks Inc., Natick, MA, USA) in order to create median images.

3.3.1 Median images from half

In order to assess the repeatability of the free breathing protocol, median images were also created from the half of the repetitions. Thus creating the images median 1-12 and median 13-24. These images can also be assessed as the median images from the first and second half of the scanning, since repetition is the outer loop, hence gives the ability to see if any changes within the time frame of the scan.

3.4 SNR

SNR were calculated, using Equation 1.10, for all b-value 0, 200 and 800 for both imaging protocols; respiratory triggered and free breathing. Additionally the free breathing median 1-12 and median 13-24 SNR were calculated. The signal was measured in a ROI within pancreas. A in-house made Matlab program, Mripsto2, created by Pål Erik Goa, was used to draw in the ROI and calculate means and standard deviation. The ROI's were placed by an individual with no medical training, but radiographers were consulted in the process. The ROI was drawn in one slice, where the pancreatic body were visible, and drawn to fill the entire section of pancreas visible in this slice. The ROI was placed in approximately the same place in both the respiratory triggered and free breathing images, making them as similar as possible. The same ROI was applied for all free breathing median images. A paired t-test between the size of the ROI placed in the respiratory triggered images and the free breathing images was conducted in Matlab. The noise was measured in a region in the air above the abdomen, the region was in the same slice as the ROI of pancreas and the same region was applied on all images from one patient.
A paired t-test was conducted in Matlab for all three b-values, between respiratory triggered and free breathing, and between the free median 1-24 and both median 1-12 and median 13-24, in addition the paired t-test were conducted between median 1-12 and median 13-24.
Additionally the ratio between the different was calculated, in order get a quantitative measure of the difference.

3.5 Ghosting

The ghosting were assessed quantitatively by the percent-signal ghosting test, as mentioned in section 1.3.1. The Matlab program Mripsto2 was applied in order to draw in ROI in both sides, top, bottom and the pancreas. Identical ROI on top, bottom and sides were applied to both the respiratory triggered and free breathing images. The ROI in pancreas applied the same ROI as in SNR analysis. The Equation 1.4 was then applied.

3.6 ADC map

Two ADC maps were created for the free breathing and respiratory triggered in Matlab, programming code in Appendix A.1. One ADC map was in the range of low diffusion weighing, created from b-values 0 and 200, $ADC_{0,200}$, while the other was in the range of medium diffusion weighing, created from images with b-values 200 and 800, $ADC_{200,800}$. In order to circumvent noise the voxels where the signal was higher in the image with most diffusion weighting were set to 0 in the ADC map. In addition a threshold value was set; if the voxel in the images with b-value 0 was under this threshold value, the corresponding voxel value in the ADC map was set to 0. ADC maps with threshold value, 10, 20 and 50 were created. The ADC maps were qualitatively assessed by a person with no medical training, in order to chose a threshold value were adequate noise was removed without loosing information of interest in the images.

3.6.1 Sharpness

The sharpness in both $ADC_{0,200}$- and $ADC_{200,800}$ map, were assessed by drawing a lines through the body of the pancreas, in both PE and RO direction, and obtaining the voxel value along the line in order to create a plot of these. The sharpness in the ADC maps was considered to be more relevant than the sharpness in the DWI when the purpose of the images is to create RED maps. The PE and RO direction was chosen in order to make it similar over the population, so that motion in either direction do not contribute different among the study population.

The open software ImageJ was applied in the creation of the line and obtaining of the voxel values. Two lines were created, one in the read out direction, horizontally, and one in the frequency encoding direction, vertically. The same lines were applied for all the ADC maps in one patient, and the line was drawn so that it entered and exit pancreas in both images. The image slice was chosen so that the anatomical location were approximately the same in free breathing and respiratory triggered images.

3.7 RED map

For patient 8 the $ADC_{0,200}$ and $ADC_{200,800}$ were created similar as to all the other patients. Whit Matlab the RED map was then created from these ADC maps with application of Equation 1.9 in all voxels for both protocols. The map was created to be colour map in order to make it more interpretable.

CHAPTER 4

RESULTS

4.1 Image quality

Images from patient 5 is chosen to be shown as an example of the images obtained with the different protocols. The quality of the images for this patient is representative for the images in the entire study population. Subsequent all MR images displayed are from patient 5 unless else is stated.

In Figure 4.1 a slice, for b-value 0, 200 and 800, from the respiratory triggered imaging is shown. These images are mean images created automatic during imaging. The corresponding slice from the free breathing imaging is shown in Figure 4.2. The free breathing obtained images are median images created manually after acquisition. The free breathing images seems to have a more smeared signal then the respiratory triggered images.

In Figure 4.3 and 4.4 the corresponding images to Figure 4.2 is shown, these images are also median images created from the free breathing obtained images, but Figure 4.3 are the median of the 1-12 images while Figure 4.4 are the median of the 13-24 image. As expected the median images from 12 images have appear to have a more smeared signal then the median image from 24 images.

4.1.1 Signal to Noise Ratio

The ROI created in the pancreas had an area of 204 ± 79.65 voxels for respiratory triggered images and 192.43 ± 75.50 voxels for the free breathing images. However not a significant difference (p=0.19).

As seen in Figure 4.5 the SNR is significant larger in the respiratory triggered images than free breathing images (p<0.01 for all diffusion weightings; b-value 0, 200 and 800). In patient 2 the correct protocol for respiratory triggering was not conducted and images with b-value 200 were not obtained. Thus paired *t*-test for images of b-value 200 only included values from 6 patients while the rest included values from all 7 patients. The mean SNR

for the respiratory triggered images were 2.10, 2.00 and 1.47 higher than the free breathing images, for b-value 0, 200 and 800 respectively.
The free breathing median images from 24 original images had SNR that were significant higher than both median images from 12 original images, ($p<0.01$ for b value 0 and 200, $p<0.05$ for b-value 800). The mean SNR in median 1-24 were 1.26, 1.15 and 1.19 the mean SNR in the median 1-12 and 1.21, 1.20 and 1.17 the mean SNR in median 13-24, for b-value 0, 200 and 800 respectively. There was no significant difference ($p=0.31$, 0.26, 0.52) between the free breathing median 1-12 and median 13-24 images.

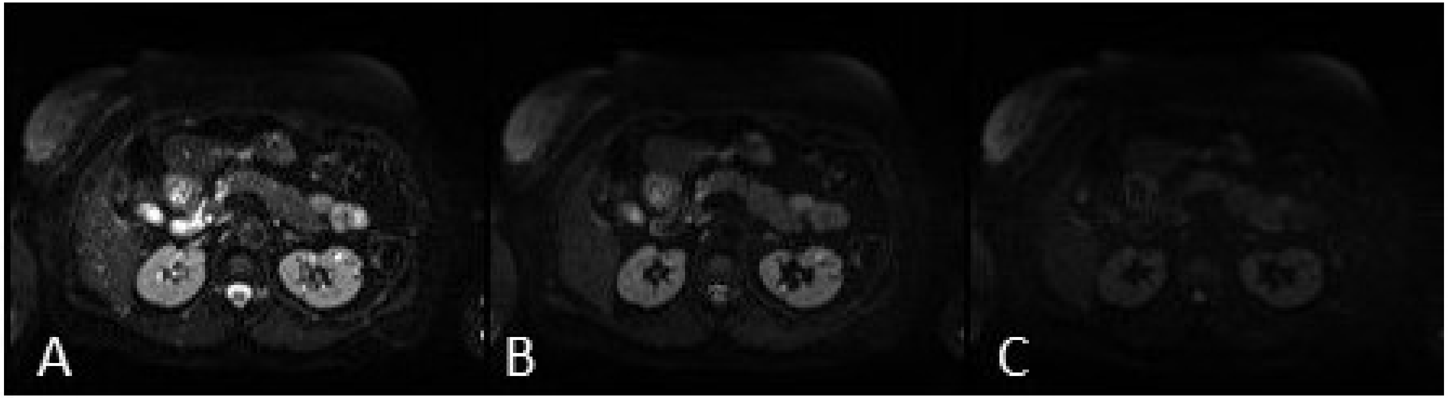

Figure 4.1: Slice from diffusion weighted images obtained with the respiratory triggered protocol in patient 5, b-value 0 (A), 200 (B) and 800 (c)

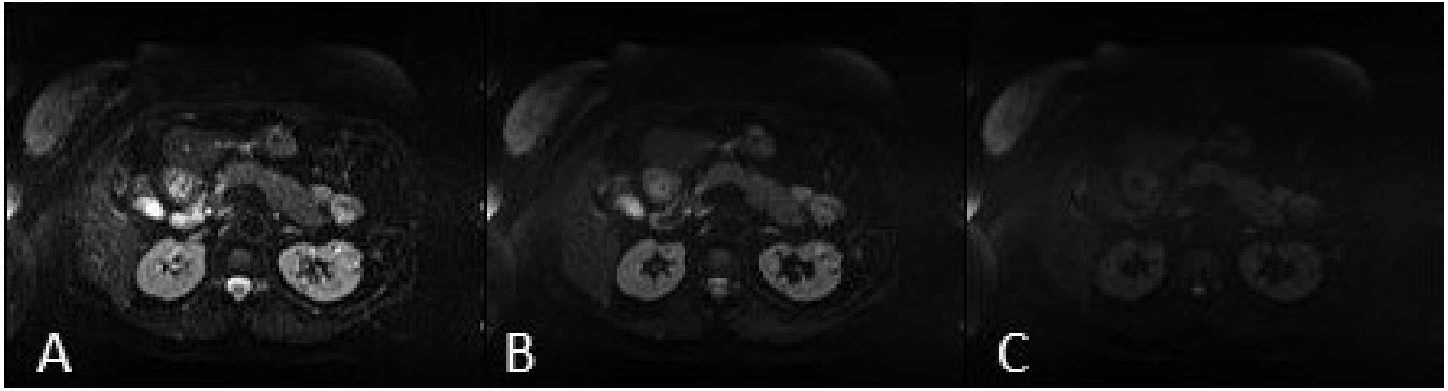

Figure 4.2: Slice from diffusion weighted images obtained with the free breathing protocol in patient 5, b-value 0 (A), 200 (B) and 800 (c). The images are created as a median from all 24 original images.

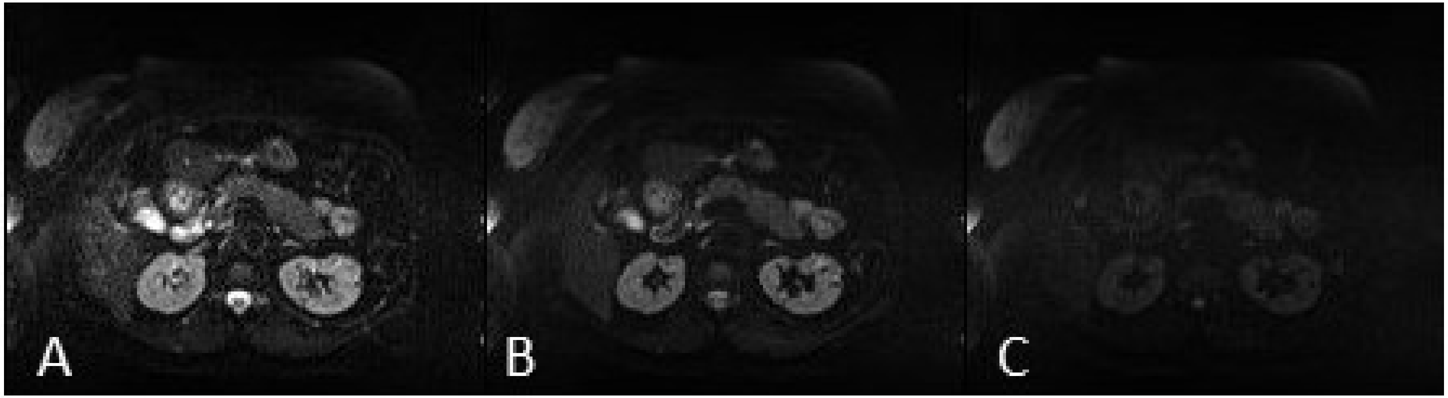

Figure 4.3: Slice from diffusion weighted images obtained with the free breathing protocol in patient 5, b-value 0 (A), 200 (B) and 800 (c). The images are created as a median from original image 1-12.

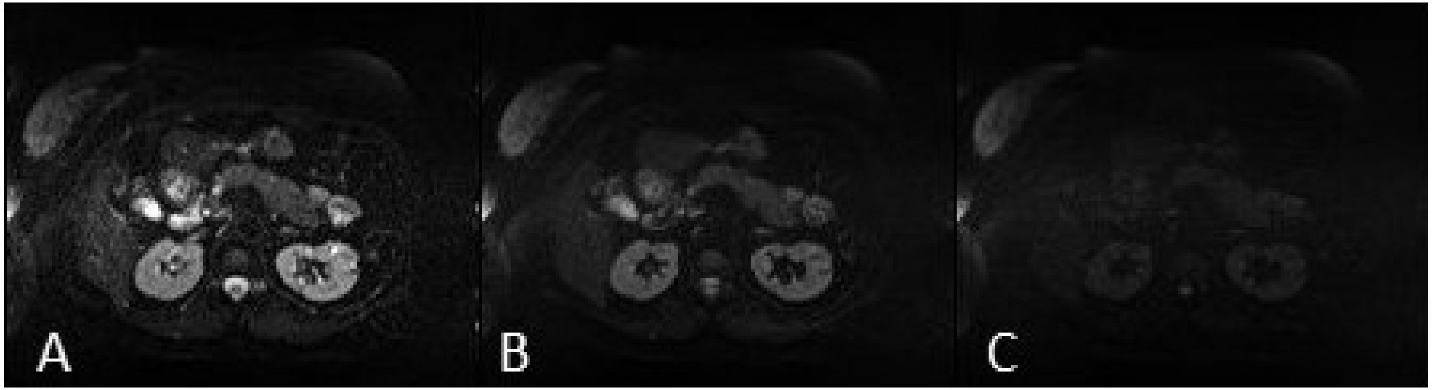

Figure 4.4: Slice from diffusion weighted images obtained with the free breathing protocol in patient 5, b-value 0 (A), 200 (B) and 800 (c). The images are created as a median from original image 13-24.

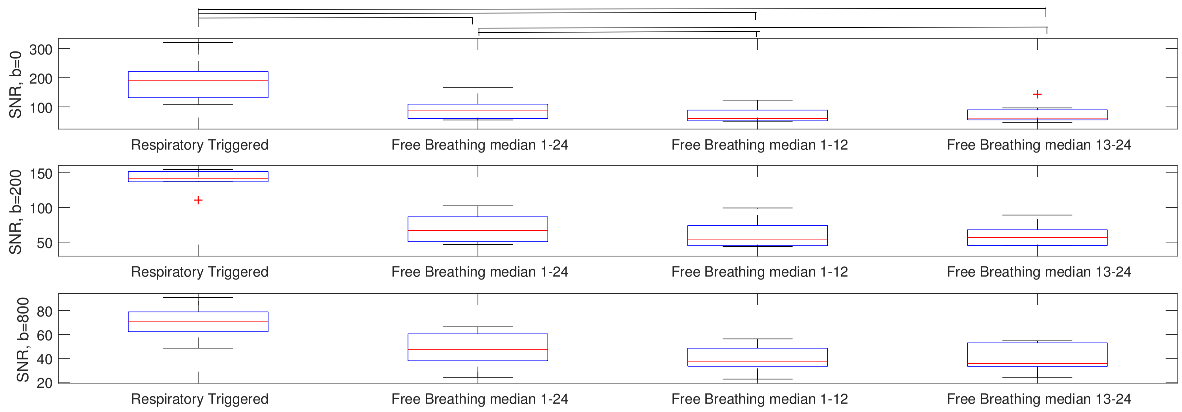

Figure 4.5: Boxplot for the SNR in the images from the respiratory triggered protocol and the free breathing protocol, with median images from 1-24, 1-12 and 13-24 from the latter protocol. The boxplot includes all diffusion weightings conducted in the thesis: b-values 0, 200 and 800. The line at the top indicate the images that have significant difference in SNR, which are the similar at all b-values.

4.1.2 Ghosting

The FOV chosen were so small that most patients filled the image horizontally, hence making the percentage-signal ghosting test impossible to applied. Patient 2 and 6 were slim enough that the images have regions on both sides in addition to top and bottom, and the percentage-signal ghosting test were applied on these two patient, in all the different b-values, 0 and 800 for patient 2, and 0, 200 and 800 for patient 6. The resulting ghosting ratios are displayed in Table 4.1, where also the ratio between the ghosting ratios are displayed. The ghosting ratio increases with diffusion weighing in both protocols. Respiratory triggered images have a lower ghosting ratio in all the images.

Table 4.1: The ghosting ratio from the percentage signal ghosting test applied to images with different diffusion weighing and different imaging protocols in two patients, Patient 2 and Patient 6. The ratio between the ghosting ratios are also displayed. Identical ROI were applied for all b-values and both imaging protocols for top, bottom, left, right, but ROI in the pancreas were slightly different in pancreas, but tried to get the same.

	b-value	Respiratory Triggered	Free Breathing	RT-FB Ratio
Patient 6	0	0.07	0.14	0.50
	200	0.10	0.23	0.42
	800	0.25	0.42	0.60
Patient 2	0	0.03	0.06	0.40
	800	0.10	0.29	0.36

4.1.3 Threshold in ADC maps

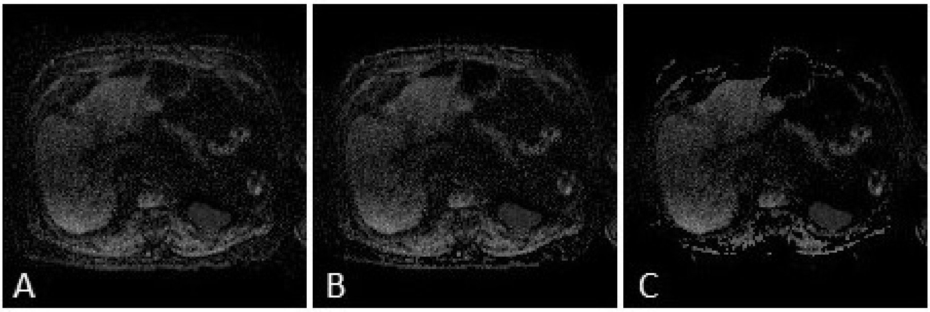

Figure 4.6: Three versions of slice from the $ADC_{200,800}$ map in patient 3 obtained with the free breathing protocol. The versions differ in the threshold value set when creating the $ADC_{200,800}$ map, and the threshold values are 10 (A), 20 (B) and 50 (C).

In Figure 4.6 a slice of the the free breathing $ADC_{200,800}$ map, created with the different threshold values 10, 20 and 50 are shown. From the figure it is clear that the amount of information put in the resulting ADC map decrease with an increasing threshold value. In the $ADC_{200,800}$ map created with threshold value 10 some noise is still present in the regions outside the body, while the $ADC_{200,800}$ map with threshold value 50 the outline of the body starts to disappear and visible black regions are showing on the inside the body. In $ADC_{200,800}$ map with threshold value 20 the noise outside the body is almost eliminated, but the outline of the body is still present and the loss of signal inside the body is not manifested as regions of black as it is in the $ADC_{200,800}$ map with threshold value 50.

4.1.4 ADC maps

An image slice from the $ADC_{0,200}$- and $ADC_{200,800}$ maps with threshold value 20, for respiratory triggered and free breathing images in patient 5 is shown in Figure 4.7 and 4.8. In the $ADC_{0,200}$ maps less noise is removed in the free breathing images than the respiratory triggered images.

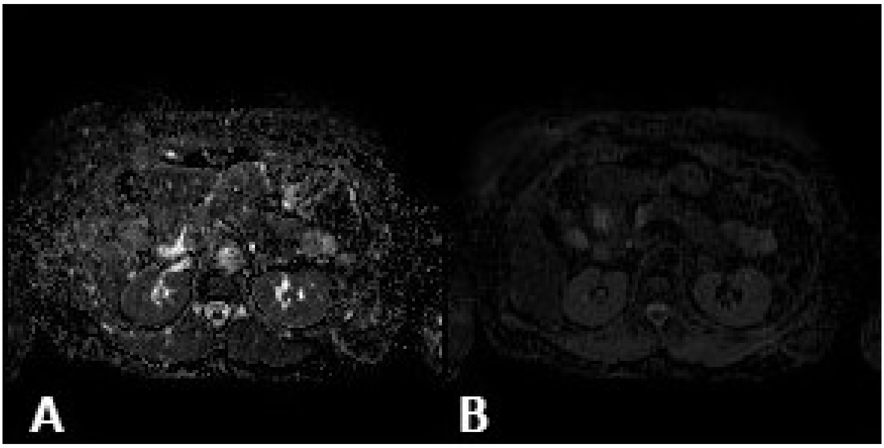

Figure 4.7: The corresponding slice in $ADC_{0,200}$ (A) and $ADC_{200,800}$ (B) created from the images obtained with the respiratory triggered protocol in patient 5.

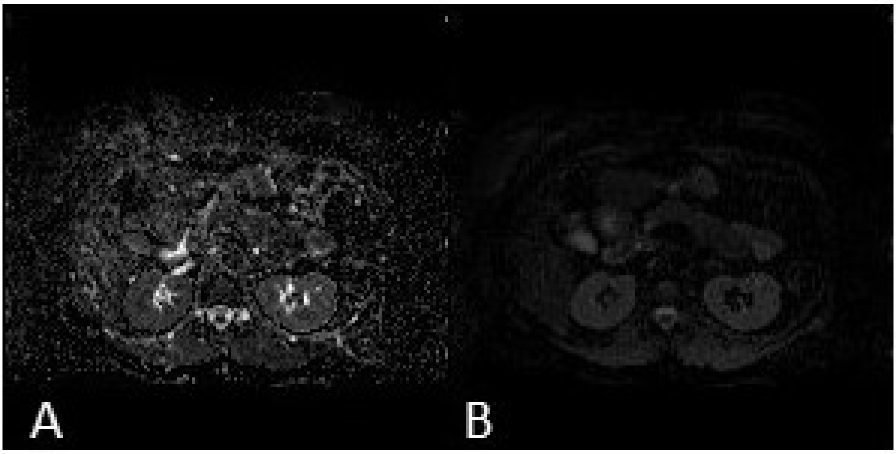

Figure 4.8: The corresponding slice in $ADC_{0,200}$ (A) and $ADC_{200,800}$ (B) created from the images obtained with the free breathing protocol in patient 5.

Sharpness

In Figures 4.9, 4.10, 4.11 and 4.12 the plots of ADC values from a line through the body of pancreas is shown. In Figure 4.9 and 4.10 the line is placed, in PE direction and RO direction respectively, in the $\mathrm{ADC}_{0,200}$ map. In Figure 4.11 and 4.12 the line is placed, in PE direction and RO direction respectively, in the $\mathrm{ADC}_{200,800}$ map. Plots of the ADC values from lines in PE and RO direction through pancreas in $\mathrm{ADC}_{0,200}$ and $\mathrm{ADC}_{200,800}$ in all patients are displayed in Appendix A.4, A.5, A.6, and A.7.

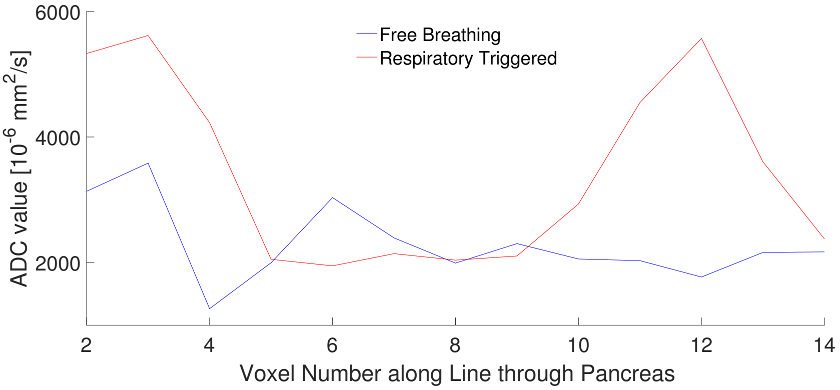

Figure 4.9: Plot of $\mathrm{ADC}_{0,200}$ along a line running through the pancreas in the phase encoding direction for both the free breathing (blue) and respiratory triggered (red) protocol in patient 5.

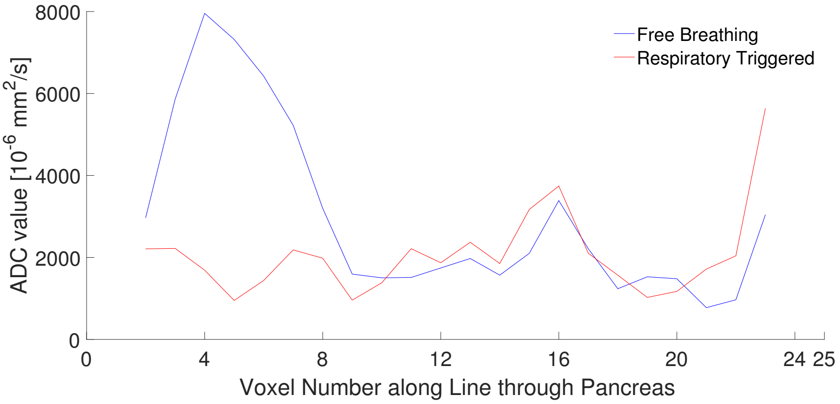

Figure 4.10: Plot of $\mathrm{ADC}_{0,200}$ along a line running through the pancreas in the read out direction for both the free breathing (blue) and respiratory triggered (red) protocol in patient 5.

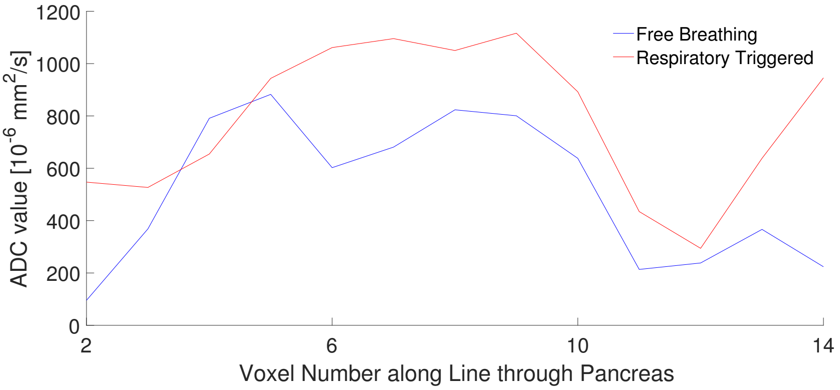

Figure 4.11: Plot of $\text{ADC}_{200,800}$ along a line running through the pancreas in the phase encoding direction for both the free breathing (blue) and respiratory triggered (red) protocol in patient 5.

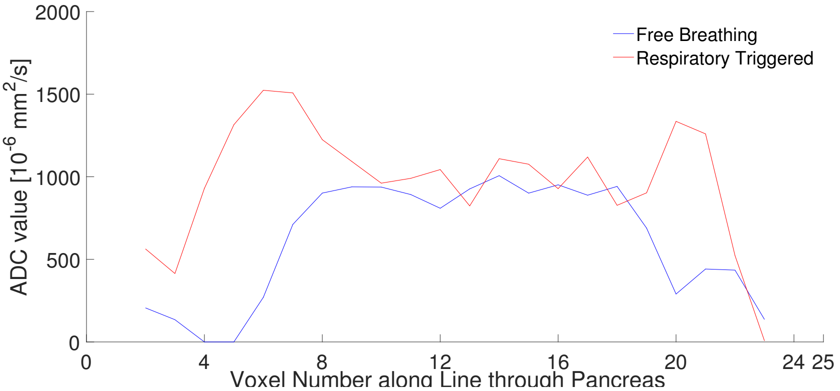

Figure 4.12: Plot of $\text{ADC}_{200,800}$ along a line running through the pancreas in the read out direction for both the free breathing (blue) and respiratory triggered (red) protocol in patient 5.

In Figure 4.9 and 4.10 it is clear to see that the pancreas do not have an $\text{ADC}_{0,200}$ differing much from the neighbouring tissues in neither RO or PE direction. The $\text{ADC}_{200,800}$ of the pancreas have greater contrast to the surrounding tissues. The transition is generally sharper in the $\text{ADC}_{200,800}$ map for the respiratory triggered protocol for both RO and PE direction. This applies for both transition into and out of the pancreas, with the transition into pancreas in patient 5 being the only exception.

For the $\text{ADC}_{200,800}$ maps for both the free breathing protocol and the respiratory triggered protocol the transition is sharper in the RO direction than in the PE direction, though the difference is larger in the free breathing protocol.

The transition into and out of the pancreas is not located in same position this is evident in the plots in Figure 4.11 and 4.12. The transition is located at different position along the line for the respiratory triggered protocol and the free breathing protocol. The pancreas is wider in the $ADC_{200,800}$ maps for respiratory triggered protocol than in the $ADC_{200,800}$ maps for the free breathing protocol. This is generally true for all patients with exception in patient 1 where the pancreas appear wider in the $ADC_{200,800}$ map for the free breathing protocol. These differences are clear even though the exact same line is applied in $ADC_{200,800}$ maps for both protocols and the slices are chosen to correspond to same anatomical location.

4.1.5 RED map

The RED map calculated from all values in both the free breathing images and the respiratory triggered images is shown in Figure 4.13. In this image the the background is set to be black, while all RED values above 400 are set to be burgundy. The RED map for the respiratory triggered protocol has less values above 400 and more values within the range of 1-200 than the RED map for the free breathing protocol. The body, pancreas and the tumor suspicious tissue is more apparent in the respiratory triggered RED map.

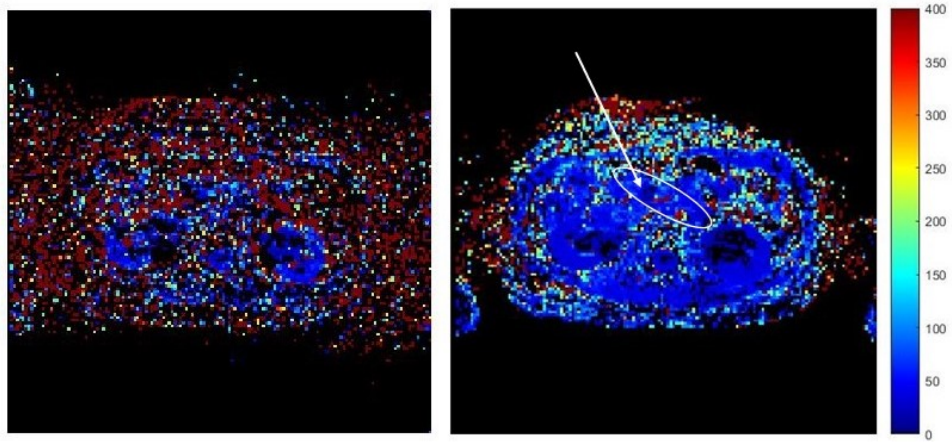

Figure 4.13: A RED map created from images obtained with the respiratory triggered protocol, to the left, and free breathing protocol, to the right, in patient 8. In this slice the body and the head of the pancreas is visible, and clearly visible in the RED map for respiratory triggered protocol, where it is with a ellipsoid, tumor suspicious tissue is also visible here and marked with an arrow.

CHAPTER 5

DISCUSSION

When creating a new protocol that is in order to be implemented clinically there are several things to consider such as if the new protocol actually is an improvement, if the image quality is adequate so that the information can be correctly interpreted, if the protocol is applicable in the clinical setting, if the protocol is compatible with the hardware and software available, and if not if the modifications are feasible in terms of cost and time. In the end the new protocol might end up as a trade off between the different aspects, perhaps the protocol is time consuming, but the image quality is superior to all other alternatives an therefor the protocol is chosen.

5.1 Image Quality

The quality of the image is an important aspects of the protocol, if the quality is inadequate, and the information is lost, the imaging is pointless. The pancreas is subject to a range of motion caused by respiration and peristalsis, thus one of the main challenges is to get images with sufficient quality. Peristalsis is handled by administration of Buscopan, which anaesthetises the intestine [10].

The main scope of this thesis is to compare the image quality of images obtained with two different protocols; one where imaging is conducted while the patient breaths freely and the images are created as a median, and one where the imaging is respiratory triggered and images are created as an average, in order to conclude which protocol creates the best images, and should be continued in the project of implementing a new DWI protocol for differing pancreatic cancer and pancreatitis.

In both free breathing and respiratory triggered protocol, three b-values where chosen to be utilised. Since the protocols were added to an regular MR examination of pancreas, the addition of two protocols where 10 b-values, as required for IVIM [19], would be impossible. Thus the RED model was chosen, hence giving both the possibility to compare the protocols and assess if they are compatible the RED model. Even if RED had been shown to be completely useless in the pancreas, the protocol that is superior could still be further developed as an IVIM protocol.

5.1.1 SNR

The SNR are significant higher in the respiratory triggered images than the free breathing images for all diffusion weighting, though with decreasing magnitude as the diffusion weighting increases. This is despite the fact that the respiratory triggered images were created from 12 original images while the free breathing images were created from 24 original images. Additionally the free breathing images were median images unlike the respiratory triggered images that were mean images. Hence the extreme values should have a greater impact on the respiratory triggered images than the free breathing images; the motion during imaging is more apparent in the respiratory triggered images than the free breathing images. Though the result indicate that the respiratory triggering limits the motion range to such an extent that it outperforms the median filtering of the free breathing protocol.

In the free breathing images there is a significant increase in SNR when the median images are created from 24 original images as opposed to 12 original images. However the magnitude of the increase is not that large. When doubling the number of images the SNR in a mean image is expected to increase with $\sqrt{2}$ [27]. Median is a more stable value, not inflicted in same manner by extreme values, and SNR will not have the same increase with increasing the number of repetitions. Hence it is not just to increase the number of repetitions within the free breathing protocol in order to get the same SNR as in the respiratory triggered images.

There is no significant difference between the median 1-12, and median 13-24. This is as expected an confirms the repeatability [29]. A significant difference could indicate a serious error on the scanner, or that patients were unable to remain still through out the entire scan. Which would be unlikely with a scanning time of roughly 3 minutes, which is within the normal duration of a clinical scanning.

The time requirement is one of the features of a protocol that is important in a clinical setting. The respiratory triggered imaging takes approximately the twice the amount of time of the free breathing imaging. However the time span of a respiratory triggered imaging is ultimately dependent on the patient and its breathing pattern. A continuous and even breathing pattern generates the best images. If the patient have an uneven breathing pattern the duration of the imaging increases. Which in turn could effect the imaging quality, giving room for more motion and conducting imaging in a larger part of the cycle then planed. If a patient has a reduced general condition or is very uncomfortable during the examination the breathing, and the image quality, could be affected. Thus the quality of the respiratory triggered images rely more on the patients then in a free breathing protocol, and might give more variation in the quality.

The ROI placed in pancreas was not the exact same for the respiratory triggered protocol and the free breathing protocol. Ideally the pancreas should be similar in images from both protocols and one ROI should fit in both. However when drawing the ROI's, the same ROI did not seem suitable for the pancreas in both images. An effort was made to find the corresponding anatomical location, this might have been unsuccessfully due to motion between the protocols or just inexperience of the person placing the ROI. This would give a signal that originate from different areas of the pancreas, and making a comparison faulted. However it is unlikely that displacement between the two protocols would favour one of the protocols.

The size of the ROI area was general smaller, however not significantly, in free breathing obtained images, with patient 7 as the only exception. The ROI was drawn in to include the entire part of pancreas visible in the slice and the similar approach was applied for both protocols. Variation in ROI area size could be due to different anatomical location. Variation in size could originate from differences in median and mean creation of images. The median images smooths the signal in the periphery of the pancreas making it appear smaller than in mean images. This could affect the sensitivity of detection in the periphery of the pancreas. Even if the difference is not significant it can be kept in mind when further developing protocol.

5.1.2 Ghosting

The percentage-signal ghosting test is originally a test applied on phantoms while conducting quality control of a scanner. The ROI is set to a large region within the phantom, thus the signal recorded as ghost in the regions outside is the actually originate from the ROI, making the result of the test an actual percentage of the signal that is displaced in ghosts [12]. In this study the ROI is set to the pancreas, which ghosts would be located inside the body. Subsequent the ghosting ratio derived with equation 1.4 is not an actual ghosting ratio. Thus the calculated ratio itself is without meaning and can not be extracted and applied in any other studier. However it gives a value that is similar for both protocols and can be applied in comparing the degree of ghosting in images obtained with different protocols in the same patient.
When looking at the images, there are no clearly visible ghosts of the pancreas in images from either of the protocols. This might be due the intermediate signal intensity of the pancreas, thus the ghosting rather appear as a smearing of the signal. Visually comparing images from the two protocol, the signal in the free breathing images is more smeared than the signal in the respiratory triggered obtained images.

The ghosting ratios derived by the percentage-signal ghosting test also show lower degree of ghosting in the respiratory triggered obtained images than the free breathing obtained images. However only the images from two patients meets the criteria in order to assess the ghosting by the percentage-signal ghosting test. Thus these results may not be representative for the actual ghosting in images obtained with the different protocols.
It is more difficult to obtain images with high image quality in obese patients. The fat suppression is less successful and this, in addition to other effects, make the image quality degraded including an increased ghosting. Thus images from the slimmest patients within the study might not give a ghosting that is true for the population.

5.1.3 Threshold ADC maps

In order to make the ADC maps more interpretable a threshold is set, and all values below this threshold value is set to 0. In the ADC map the threshold is set in the DW-image with b-value 0, instead of the actual ADC maps. When selecting the value for the threshold it is important to find a value that removes noise without removing true signal and information. In the ADC maps shown in Figure 4.6 the quantity of ADC values within a map clearly decreases with the increasing threshold value. When the threshold is set to 10, there is still much noise visible in the ADC map. On the other hand when the threshold is set to 50 not much visible noise is present but the signal inside the anatomy is lost, changing the appearance of the organs, indicating that some true information could be lost. Therefor the threshold value 20 was chosen, it seem to be a good choice of value, removing most of the visible noise but remaining the appearance of the organs.
When setting a threshold of 20 in the ADC maps from free breathing protocol and the respiratory triggered protocol, the noise removal seem most successful in the respiratory triggered ADC maps: the area surrounding the body is mainly set to zero while the regions inside the body seem to be mostly unaltered and without suspicious black regions, corresponding to the value 0. In the ADC maps from the free breathing protocol the noise outside the body is much more present, and more black regions are visible in the anatomy. This is especially apparent in the $\mathrm{ADC}_{0,200}$ maps, while the $\mathrm{ADC}_{200,800}$ maps form the two protocols are harder to visually separate on quality. These observation is in agreement with the lower SNR in the free breathing images then in the respiratory triggered images. A higher SNR will make it easier to set a cut off between the noise and the signal.

5.1.4 Sharpness

In $\mathrm{ADC}_{0,200}$, in both PE and RO direction, there is no clear transition into or out from the pancreas, with a couple exception: patient 1 in PE direction and patient 3 in RO direction. In order to assess the sharpness between zones in an image the property displayed in the image, here the $\mathrm{ADC}_{0,200}$, has to differ between the zones. In $\mathrm{ADC}_{0,200}$ the pseudo-diffusion, perfusion, is a great contribution to the ADC values [18]. In these $\mathrm{ADC}_{0,200}$ maps the pancreas and the neighbouring tissues seem to have similar values for $\mathrm{ADC}_{0,200}$, resulting in no transition between the different zones. Looking at the $\mathrm{ADC}_{0,200}$ maps the pancreas is even hard to identify. Thus the lineplots from line throughout pancreas is useless in evaluating the sharpness of the $\mathrm{ADC}_{0,200}$ maps from the free breathing and respiratory triggered protocol. The sharpness of the $\mathrm{ADC}_{0,200}$ map could be evaluated in different part of the image. However the protocol is for imaging of the pancreas and the difference in motion experienced by the different organs makes sharpness in any other part of the image irrelevant.

In $\mathrm{ADC}_{200,800}$ the contribution from perfusion less profound and the pancreas appear to have greater contrast to its surrounding tissues. Thus the sharpness in the $\mathrm{ADC}_{200,800}$ from free breathing images and respiratory triggered images can be compared. The $\mathrm{ADC}_{200,800}$ map from the respiratory triggered protocol generally have a higher sharpness then the $\mathrm{ADC}_{200,800}$ map from the free breathing protocol. This is true for both transition into and out of the pancreas in both PE and RO direction. The only exception being the transition into pancreas in PE direction for patient 5. The sharpness can vary within the image, and a selected position can give a sharpness that does not represent the entire image. The better sharpness in the ADC maps from the respiratory triggerd protocol is in compliance with the earlier detection, that the respiratory triggered images have higher SNR and less ghosting present than the free breathing images.

As expected the sharpness is lower in the PE direction than in the RO direction. This is especially evident in the $\mathrm{ADC}_{200,800}$ map for free breathing protocol, where even transition is invisible in the line plots from a couple of patients. Hence the difference in the sharpness between the two protocols is even larger in the PE direction.

In line plots for $\mathrm{ADC}_{200,800}$ in Appendix A.5 and A.7 it is clear to see that the transition into and out of the pancreas is not located at the same place along the line for both protocols, generally the free breathing have narrower pancreas. This is the same effect as seen in smaller area of ROIs in the free breathing images than the respiratory triggered images, this was discussed in Section 5.1.1. The reason is believed to originate in the differences with creation of images as a median or a mean.

5.1.5 RED map

In the RED maps the difference in quality between the two protocols are even more evident than in any of the ADC maps or the DW images. The RED map for the free breathing protocol clearly has a lot of noise in the map simultaneously some signal in the region of the zone of the pancreas seem to have been removed by the threshold in ADC map. In the RED map from the respiratory triggered protocol the RED values in the pancreas remain, it is even identifiable in the images, the same is true for the tumor suspicious tissue within the pancreas head. The noise is less present in the RED map for the respiratory triggered protocol, however a cut off value to remove this from the image could improve the RED map, make it more interpretable. Looking at the RED map the respiratory triggered protocol is superior the free breathing protocol. The free breathing obtained images seem to have a image quality too poor to be used in creation of RED maps.

5.2 Is RED a good parameter in evaluation of pancreatic cancer and pancreatitis?

RED is a fairly new developed model that instead of separating the diffusion and perfusion, such as in IVIM model, calculated the relation between the perfusion and the diffusion [20]. This relation makes the imaging procedure much easier, when three diffusion weightings are required in contrast to 10 diffusion weighting which is a minimum in an IVIM imaging, in order to get good values [15]. A DW imaging with 10 b-values give a long duration of the scan, especially when the imaging is respiratory triggered, perhaps so long that it is not an option in the clinic.

In many types of cancer the perfusion is increased while the diffusion is decreased compared to the healthy tissue. Resulting in a high increase in the RED value, which easier can be separated from the healthy tissue than the traditional ADC values.
However in PDAC, the most common type pancreatic cancer, f_p decreases, while D_t is not significant changed [22] [23]. Subsequent the RED value decreases, probably with a smaller magnitude than the increase expected in many cancer types .

Chronic pancreatitis have a f_p significantly higher than PDAC, but also significantly lower than healthy pancreatic tissue. The D_t for pancreatitis does not vary significantly from either healthy pancreas or PDAC [4]. Resulting in a intermediate RED value. If the RED value is significantly different between chronic pancreatits and PDAC is subject for further investigation. However it is probable when f_p differences are significant and perfusion parameter in RED value is closely related to the f_p . The clinical DWI-protocol at St. Olavs Hospital today create a ADC map from b-value 50, 200, 400 and 800, where there is no significant difference between PDAC and pancreatits [4]. An imaging method where there is a difference would be a helpful tool even if the difference is small and not as easy to interpret as ideally.

In studies of pancreas the f_p is the DWI-derived constant that was the best in differing PDAC and pancreatitis. Therefore f_p map from an IVIM scanning might seem to be a good solution. In addition to the time consumption of an IVIM scanning diffusion sensitive parameters f_p and D^* have a unacceptable low reproducibility [30].
Consequently the RED model seems promising as an part of a new protocol since it does not require a long scanning time and the reproducibility of ADC values, which the model is based on, is far better than the reproducibility of f_p [30].

5.3 Software Compatibility

In free breathing protocol the images are created as a median image. This is done because of the large range of motion during imaging resulting in mean images where the quality probable is too low. The creation of median images is not a function available at the scanners or in other clinical software at St. Olavs Hospital. However the original images can be retrieved after scanning and manipulated in Matlab or other software. However this gives challenges in further manipulation in clinical software. This challenge can be overcome, however it will be more labour intensive than if creation of a median images was a function in the clinical software.
The protocol for respiratory triggering apply the traditional averaging, thus being compatible with the software in its current state. Giving this protocol an advance, since the majority of the protocol can be executed with the current state clinical software. Creation of RED map is, of course, not a function available in the software. This is the same for both protocols, not giving either of them an advantage.

If software is updated in order to create median images, this function should also be applied on respiratory triggered protocols. When imaging is respiratory triggered the mean images is created during the imaging, and only these images are saved for further examination and manipulation. The more stable nature of the median value in comparison to the mean, gives hope that median images could give a better result in the respiratory triggered images. An attempt in order to create the median images from the raw data by changing the reconstruction in IDEA, a reconstruction software, was conducted. However the lack of sufficient local knowledge on IDEA made it time consuming and problematic. With the time limitations on this study, this was excluded from the thesis. However it is unlikely that a protocol that require median respiratory triggered images is included in a clinical trial when the raw data is only stored for approximately 2 days, and have to be manually retrieved from the MR-scanner while it is not scanning, making it impractical, when the scanners are in use two shifts each day, in addition to labour intensive.

CHAPTER 6

CONCLUSION AND FURTHER WORK

6.1 Conclusion

The images obtained with respiratory triggering have better image quality than the median free breathing images, with a significant improved SNR for images with all b-values, 0, 200 and 800, less ghosting is apparent, the ADC maps have a better sharpness and at the end line the RED map is better. This is despite the fact that the free breathing protocol have twice the amount of repetitions as the respiratory triggered protocol. Additionally the respiratory triggered protocol is more compatible with the software available on MR-scanner and elsewhere on St. Olavs Hospital, making a clinical trial with this protocol easier to conduct than a clinical trial with the free breathing protocol.
Based on these results the respiratory triggered protocol is the favourable protocol. Further development of a DWI pancreas protocol should be based on the respiratory triggered protocol.

Based on the results form one patient the RED model is promising when the images have the quality of the respiratory triggered images and it should be subject for further investigation.

6.2 Further Work

Further investigations has to be done on RED values in PDAC and chronic pancreatitis to establish if there actually is a significant difference in RED value between the two. Additionally a study should be conducted to see how the IVIM parameters behave in comparison to the RED value, and which gives the best differentiation of PDAC and chronic pancreatitis. Thus a study where a protocol with sufficient b-values to apply the IVIM model could be conducted in order to compare RED and IVIM, whilst evaluating the RED model in the same study.

The RED model seems promising, however it could be assessed if the creation of ADC maps from three b values instead of two improve the quality of the resulting RED map. In the images, obtained with the respiratory triggered protocol, for this study the excess b-values, from the original DWI protocol, it is possible to create $\text{ADC}_{0,50,200}$ and $\text{ADC}_{200,400,800}$ maps. Thus such an assessment can be performed without acquisition of new data.

BIBLIOGRAPHY

[1] Gillian Pocock, Christopher D Richards, and David A Richards. *Human physiology*. Oxford university press, 2013.

[2] Harold Ellis. “Anatomy of the pancreas and the spleen”. In: *Surgery (Oxford)* 31.6 (2013), pp. 263–266.

[3] Inger Kristin Larsen, ed. *Cancer in Norway 2014 - Cancer incidence, mortality, survival and prevalence in Norway*. Oslo: Cancer Registry of Norway, 2015.

[4] Miriam Klau et al. “Intravoxel incoherent motion MRI for the differentiation between mass forming chronic pancreatitis and pancreatic carcinoma”. In: *Investigative radiology* 46.1 (2011), pp. 57–63.

[5] M Takeuchi et al. “High-b-value diffusion-weighted magnetic resonance imaging of pancreatic cancer and mass-forming chronic pancreatitis: preliminary results”. In: *Acta Radiologica* 49.4 (2008), pp. 383–386.

[6] Mark A Brown and Richard C Semelka. *MRI: basic principles and applications*. John Wiley & Sons, 2011.

[7] Catherine Westbrook and Carolyn Kaut Roth. *MRI in Practice*. John Wiley & Sons, 2011.

[8] Maggie A Flower. *Webb’s physics of medical imaging*. CRC Press, 2012.

[9] Mehdi Poustchi-Amin et al. “Principles and applications of echo-planar imaging: A review for the general radiologist 1”. In: *Radiographics* 21.3 (2001), pp. 767–779.

[10] Donald W McRobbie et al. *MRI from Picture to Proton*. Cambridge university press, 2007.

[11] Mark A Griswold et al. “Generalized autocalibrating partially parallel acquisitions (GRAPPA)”. In: *Magnetic resonance in medicine* 47.6 (2002), pp. 1202–1210.

[12] American College of Radiology et al. “Phantom test guidance for the ACR MRI Accreditation Program”. In: *Reston, Va: ACR* (1998).

[13] Tiril Hillestad. "The Establishment of an Intravoxel Incoherent Motion Based MRI-Protocol for Differentiation of Focal Lesions in the Pancreas". Master thesis. NTNU, 2015.

[14] Foreningen for utgivelse av Norsk legemiddelhåndbok. *Norsk Legemiddelhandbok.* 2016. URL: `http://legemiddelhandboka.no/Legemidler/s\%C3\%B8ker/+\%2Bbuscopan/71613`.

[15] Nikolaos Kartalis et al. "Optimising diffusion-weighted MR imaging for demonstrating pancreatic cancer: a comparison of respiratory-triggered, free-breathing and breath-hold techniques". In: *European radiology* 22.10 (2012), pp. 2186–2192.

[16] Eric E Sigmund and Jens Jensen. *Basic physical principles of body diffusion-weighted MRI.* 2011.

[17] Dow-Mu Koh and David J Collins. "Diffusion-weighted MRI in the body: applications and challenges in oncology". In: *American Journal of Roentgenology* 188.6 (2007), pp. 1622–1635.

[18] Denis Le Bihan. "Intravoxel Incoherent Motion Perfusion MR Imaging: A Wake-Up Call 1". In: *Radiology* 249.3 (2008), pp. 748–752.

[19] Andreas Lemke et al. "Toward an optimal distribution of b values for intravoxel incoherent motion imaging". In: *Magnetic resonance imaging* 29.6 (2011), pp. 766–776.

[20] Jose R Teruel et al. "A Simplified Approach to Measure the Effect of the Microvasculature in Diffusion-weighted MR Imaging Applied to Breast Tumors: Preliminary Results". In: *Radiology* (2016), p. 151630.

[21] Kjetil Søreide, Heike Immervoll, and Anders Molven. "Forstadier til kreft i bukspyttkjertelen." In: (2006).

[22] Bohyun Kim et al. "Intravoxel incoherent motion diffusion-weighted imaging of the pancreas: Characterization of benign and malignant pancreatic pathologies". In: *Journal of Magnetic Resonance Imaging* (2016).

[23] Andreas Lemke et al. "Differentiation of pancreas carcinoma from healthy pancreatic tissue using multiple b-values: comparison of apparent diffusion coefficient and intravoxel incoherent motion derived parameters". In: *Investigative radiology* 44.12 (2009), pp. 769–775.

[24] Seung Soo Lee et al. "Quantitative analysis of diffusion-weighted magnetic resonance imaging of the pancreas: Usefulness in characterizing solid pancreatic masses". In: *Journal of Magnetic Resonance Imaging* 28.4 (2008), pp. 928–936.

[25] Mohamad Hamid Abo Warda, Doaa Ibrahim Hasan, and Osama Abdelaziz Elteeh. "Differentiation of Pancreatic lesions using Diffusion-Weighted MRI". In: *The Egyptian Journal of Radiology and Nuclear Medicine* 46.3 (2015), pp. 563–568.

[26] Perry Sprawls. "Image characteristics and quality". In: *Medical Physics Pub* (1995).

[27] Jerrold T Bushberg and John M Boone. *The essential physics of medical imaging*. Lippincott Williams & Wilkins, 2011.

[28] Imatest LLC. *Sharpness: What is it and how is it measured?* 2016. URL: `http://www.imatest.com/docs/sharpness/`.

[29] JW Bartlett and C Frost. "Reliability, repeatability and reproducibility: analysis of measurement errors in continuous variables". In: *Ultrasound in Obstetrics & Gynecology* 31.4 (2008), pp. 466–475.

[30] A Andreou et al. "Measurement reproducibility of perfusion fraction and pseudodiffusion coefficient derived by intravoxel incoherent motion diffusion-weighted MR imaging in normal liver and metastases". In: *European radiology* 23.2 (2013), pp. 428–434.

APPENDIX A

A.1 Matlabcode; ADC map creation

```
01.07.16 14:09   C:\Users\ingrid\Desktop\...\ADCkartFree.m    1 of 1

%S(b) = S(0) exp(-b*ADC)
%S(b)/S(0) = exp(-b*ADC)
% ln(S(b)/S(0)) = -b*ADC
B0 = medianbverdi0;
B200 = medianbverdi200;
B800 = medianbverdi800;

Bvalue1 = [0; 800];
Bvalue2 = [200; 800];

T20ADC0200 = zeros(148,148, 1, 36);
T20ADC200800 = zeros(148,148, 1, 36);

for k = 1:36
    for i = 1:148
        for j = 1:148
            if(B0(i,j,1,k) > 20 && B200(i,j,1,k)< B0(i,j,1,k))% Threshold = 20,↙
Removal of all where signal is larger in the larges b
               T20ADC0200(i,j,1,k) = (-1/200)*log(B200(i,j,1,k)/B0(i,j,1,k));
            end
            if (B0(i,j,1,k) > 20 && B800(i,j,1,k)< B200(i,j,1,k))% Threshold = 20,↙
Removal of all where signal is larger in the larges b
                T20ADC200800(i,j,1,k) = (-1/600)*log(B800(i,j,1,k)/B200(i,j,1,k));
            end
        end
    end
end


dicomwrite(uint16(T20ADC0200), 'FreePatient03ADC0200TH20');
dicomwrite(uint16(T20ADC200800), 'FreePatient03ADC200800TH20');
```

A.2 Respiratory Triggered Protocol

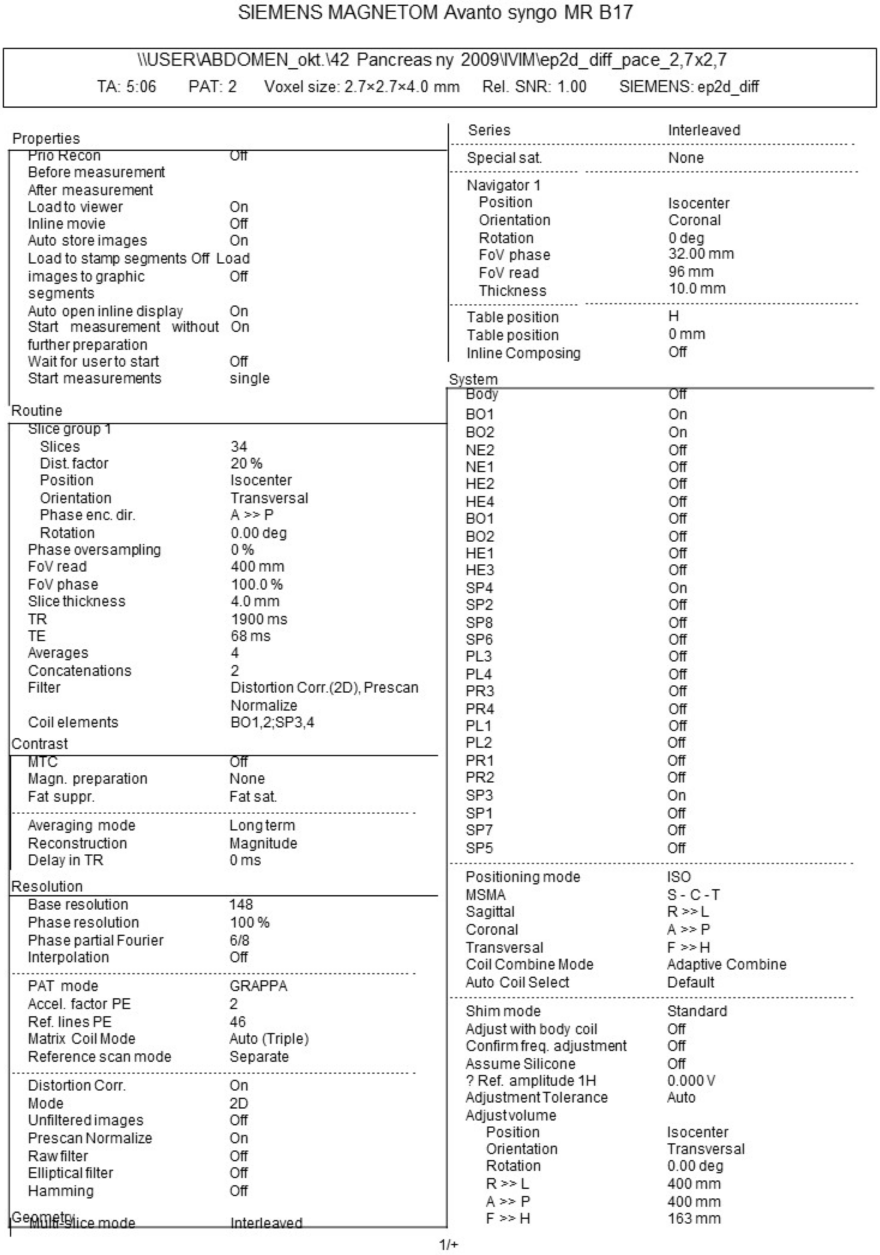

SIEMENS MAGNETOM Avanto syngo MR B17

\\USER\ABDOMEN_okt.\42 Pancreas ny 2009\IVIM\ep2d_diff_pace_2,7x2,7

TA: 5:06 PAT: 2 Voxel size: 2.7×2.7×4.0 mm Rel. SNR: 1.00 SIEMENS: ep2d_diff

Properties	
Prio Recon	Off
Before measurement	
After measurement	
Load to viewer	On
Inline movie	Off
Auto store images	On
Load to stamp segments	Off
Load images to graphic segments	Off
Auto open inline display	On
Start measurement without further preparation	On
Wait for user to start	Off
Start measurements	single
Routine	
Slice group 1	
Slices	34
Dist. factor	20 %
Position	Isocenter
Orientation	Transversal
Phase enc. dir.	A >> P
Rotation	0.00 deg
Phase oversampling	0 %
FoV read	400 mm
FoV phase	100.0 %
Slice thickness	4.0 mm
TR	1900 ms
TE	68 ms
Averages	4
Concatenations	2
Filter	Distortion Corr.(2D), Prescan Normalize
Coil elements	BO1,2;SP3,4
Contrast	
MTC	Off
Magn. preparation	None
Fat suppr.	Fat sat.
Averaging mode	Long term
Reconstruction	Magnitude
Delay in TR	0 ms
Resolution	
Base resolution	148
Phase resolution	100 %
Phase partial Fourier	6/8
Interpolation	Off
PAT mode	GRAPPA
Accel. factor PE	2
Ref. lines PE	46
Matrix Coil Mode	Auto (Triple)
Reference scan mode	Separate
Distortion Corr.	On
Mode	2D
Unfiltered images	Off
Prescan Normalize	On
Raw filter	Off
Elliptical filter	Off
Hamming	Off
Geometry	
Multi-slice mode	Interleaved

Series	Interleaved
Special sat.	None
Navigator 1	
Position	Isocenter
Orientation	Coronal
Rotation	0 deg
FoV phase	32.00 mm
FoV read	96 mm
Thickness	10.0 mm
Table position	H
Table position	0 mm
Inline Composing	Off
System	
Body	Off
BO1	On
BO2	On
NE2	Off
NE1	Off
HE2	Off
HE4	Off
BO1	Off
BO2	Off
HE1	Off
HE3	Off
SP4	On
SP2	Off
SP8	Off
SP6	Off
PL3	Off
PL4	Off
PR3	Off
PR4	Off
PL1	Off
PL2	Off
PR1	Off
PR2	Off
SP3	On
SP1	Off
SP7	Off
SP5	Off
Positioning mode	ISO
MSMA	S - C - T
Sagittal	R >> L
Coronal	A >> P
Transversal	F >> H
Coil Combine Mode	Adaptive Combine
Auto Coil Select	Default
Shim mode	Standard
Adjust with body coil	Off
Confirm freq. adjustment	Off
Assume Silicone	Off
? Ref. amplitude 1H	0.000 V
Adjustment Tolerance	Auto
Adjust volume	
Position	Isocenter
Orientation	Transversal
Rotation	0.00 deg
R >> L	400 mm
A >> P	400 mm
F >> H	163 mm

1/+

Physio

1st Signal/Mode	None
Resp. control	Trigger & Follow
Scout mode	Off
Scout TR	150 ms
Accept window ±	2.0 mm
Position accept window	Automatic
Store profile images	Off
Tracking factor	1.0
Trigger pulse	1

Diff

Diffusion mode	3-Scan Trace
Diff. weightings	5
b-value 1	0 s/mm²
b-value 2	50 s/mm²
b-value 3	200 s/mm²
b-value 4	400 s/mm²
b-value 5	800 s/mm²
Diff. weighted images	Off
Trace weighted images	On
Average ADC maps	On
Individual ADC maps	Off
FA maps	Off
Mosaic	Off
Tensor	Off
Noise level	10
Diff. directions	3

Sequence

Introduction	Off
Bandwidth	2252 Hz/Px
Free echo spacing	Off
Echo spacing	0.51 ms
EPI factor	148
RF pulse type	Normal
Gradient mode	Fast*

A.3 Free Breathing Protocol

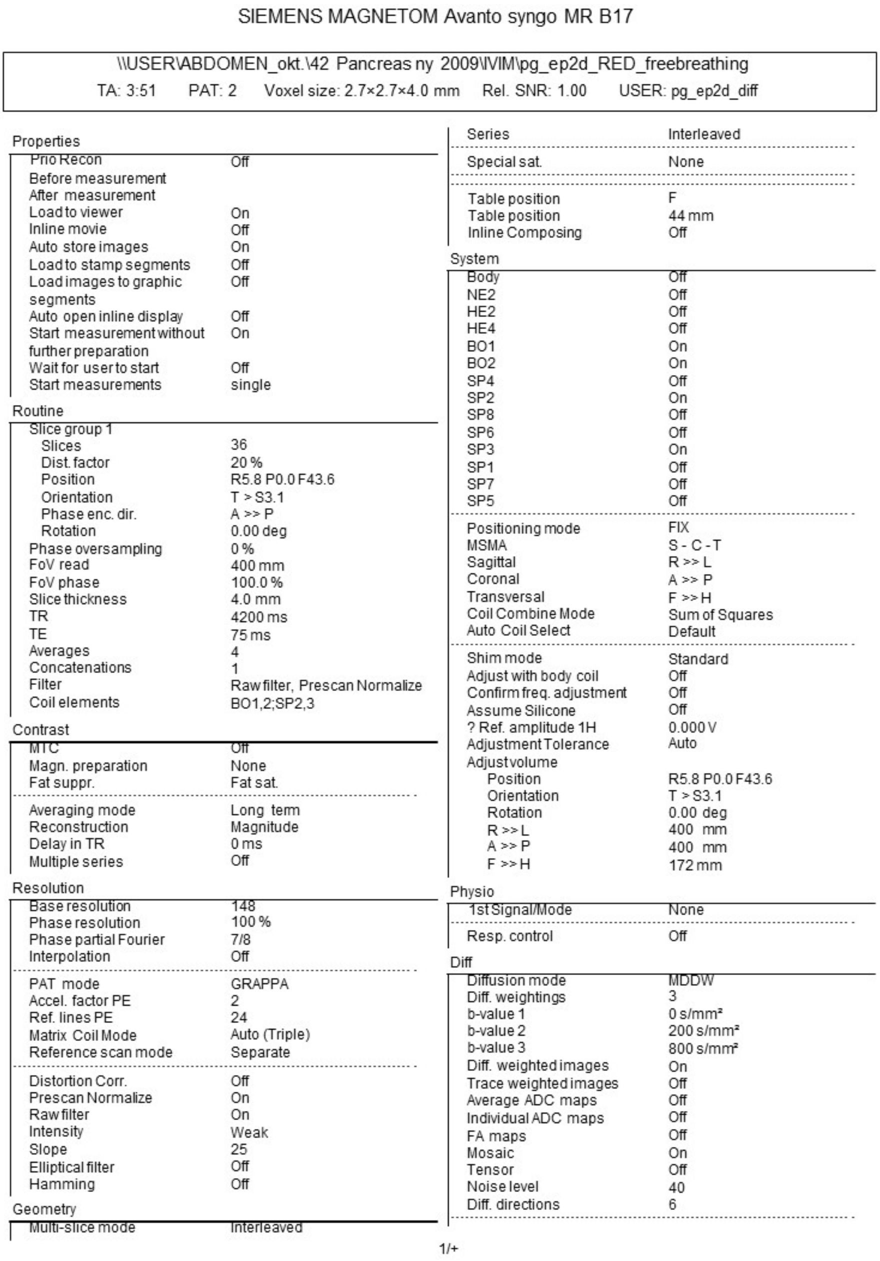

SIEMENS MAGNETOM Avanto syngo MR B17

\\USER\ABDOMEN_okt.\42 Pancreas ny 2009\IVIM\pg_ep2d_RED_freebreathing

TA: 3:51 PAT: 2 Voxel size: 2.7×2.7×4.0 mm Rel. SNR: 1.00 USER: pg_ep2d_diff

Properties

Prio Recon	Off
Before measurement	
After measurement	
Load to viewer	On
Inline movie	Off
Auto store images	On
Load to stamp segments	Off
Load images to graphic segments	Off
Auto open inline display	Off
Start measurement without further preparation	On
Wait for user to start	Off
Start measurements	single

Routine

Slice group 1	
Slices	36
Dist. factor	20 %
Position	R5.8 P0.0 F43.6
Orientation	T > S3.1
Phase enc. dir.	A >> P
Rotation	0.00 deg
Phase oversampling	0 %
FoV read	400 mm
FoV phase	100.0 %
Slice thickness	4.0 mm
TR	4200 ms
TE	75 ms
Averages	4
Concatenations	1
Filter	Raw filter, Prescan Normalize
Coil elements	BO1,2;SP2,3

Contrast

MTC	Off
Magn. preparation	None
Fat suppr.	Fat sat.
Averaging mode	Long term
Reconstruction	Magnitude
Delay in TR	0 ms
Multiple series	Off

Resolution

Base resolution	148
Phase resolution	100 %
Phase partial Fourier	7/8
Interpolation	Off
PAT mode	GRAPPA
Accel. factor PE	2
Ref. lines PE	24
Matrix Coil Mode	Auto (Triple)
Reference scan mode	Separate
Distortion Corr.	Off
Prescan Normalize	On
Raw filter	On
Intensity	Weak
Slope	25
Elliptical filter	Off
Hamming	Off

Geometry

Multi-slice mode	Interleaved
Series	Interleaved
Special sat.	None
Table position	F
Table position	44 mm
Inline Composing	Off

System

Body	Off
NE2	Off
HE2	Off
HE4	Off
BO1	On
BO2	On
SP4	Off
SP2	On
SP8	Off
SP6	Off
SP3	On
SP1	Off
SP7	Off
SP5	Off
Positioning mode	FIX
MSMA	S - C - T
Sagittal	R >> L
Coronal	A >> P
Transversal	F >> H
Coil Combine Mode	Sum of Squares
Auto Coil Select	Default
Shim mode	Standard
Adjust with body coil	Off
Confirm freq. adjustment	Off
Assume Silicone	Off
? Ref. amplitude 1H	0.000 V
Adjustment Tolerance	Auto
Adjust volume	
Position	R5.8 P0.0 F43.6
Orientation	T > S3.1
Rotation	0.00 deg
R >> L	400 mm
A >> P	400 mm
F >> H	172 mm

Physio

1st Signal/Mode	None
Resp. control	Off

Diff

Diffusion mode	MDDW
Diff. weightings	3
b-value 1	0 s/mm²
b-value 2	200 s/mm²
b-value 3	800 s/mm²
Diff. weighted images	On
Trace weighted images	Off
Average ADC maps	Off
Individual ADC maps	Off
FA maps	Off
Mosaic	On
Tensor	Off
Noise level	40
Diff. directions	6

1/+

Sequence

Introduction	Off
Bandwidth	2598 Hz/Px
Free echo spacing	Off
Echo spacing	0.52 ms
EPI factor	148
RF pulse type	Normal
Gradient mode	Fast

A.4 Plot of $\mathrm{ADC}_{0,200}$ along a Line through the Pancreas in phase encoding Direction

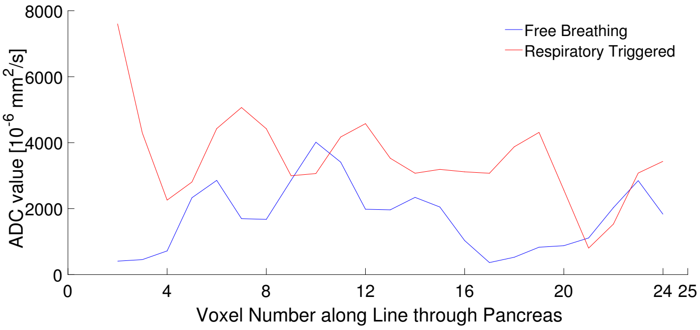

The plot of $\mathrm{ADC}_{0,200}$ values along a line though the pancreas in the PE direction in patient 1.

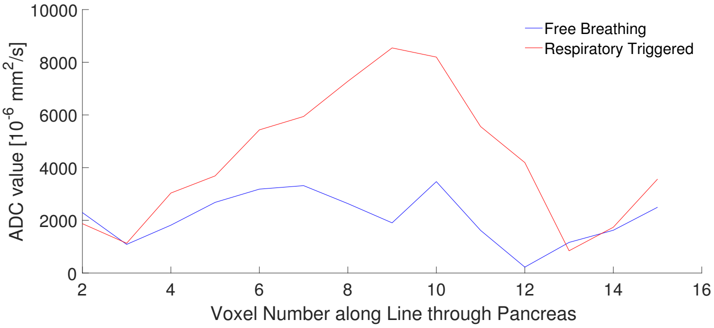

The plot of $\mathrm{ADC}_{0,200}$ values along a line though the pancreas in the PE direction in patient 3

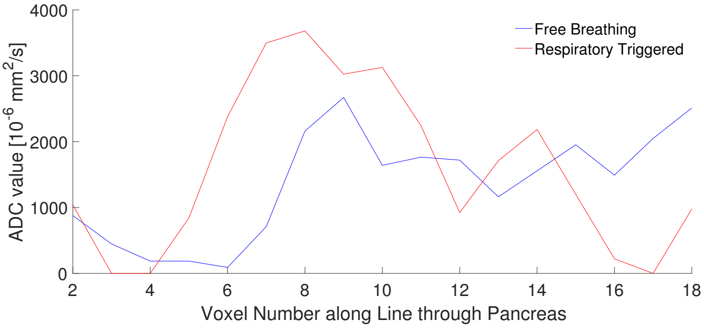

The plot of $\mathrm{ADC}_{0,200}$ values along a line though the pancreas in the PE direction in patient 4.

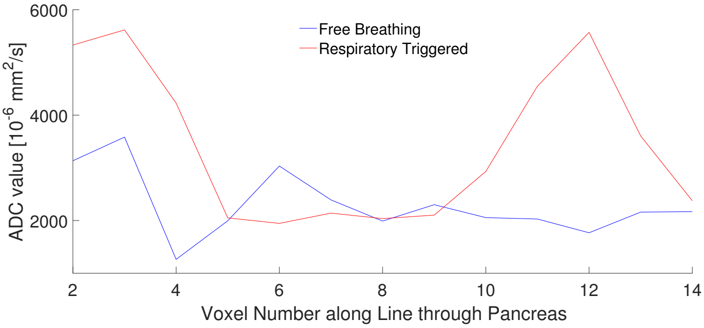

The plot of $\text{ADC}_{0,200}$ values along a line though the pancreas in the PE direction in patient 5.

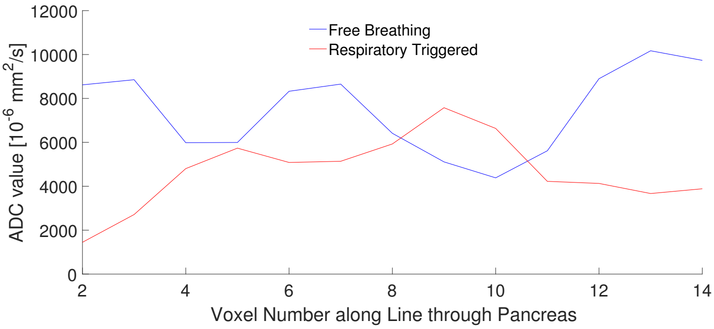

The plot of $\text{ADC}_{0,200}$ values along a line though the pancreas in the PE direction in patient 6.

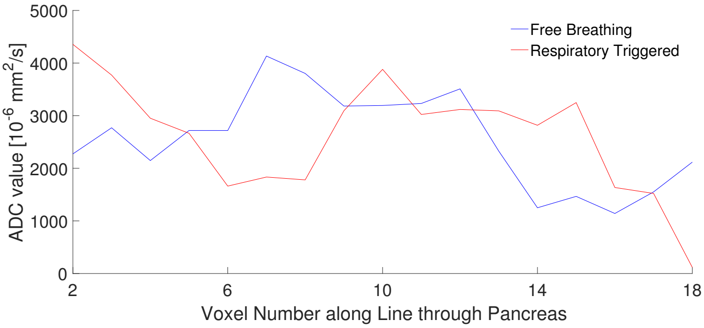

The plot of $\text{ADC}_{0,200}$ values along a line though the pancreas in the PE direction in patient 7.

A.5 Plot of ADC$_{200,800}$ along a Line through the Pancreas in phase encoding Direction

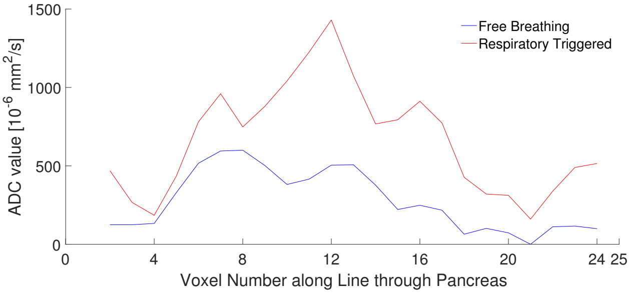

The plot of ADC$_{200,800}$ values along a line though the pancreas in the PE direction in patient 1.

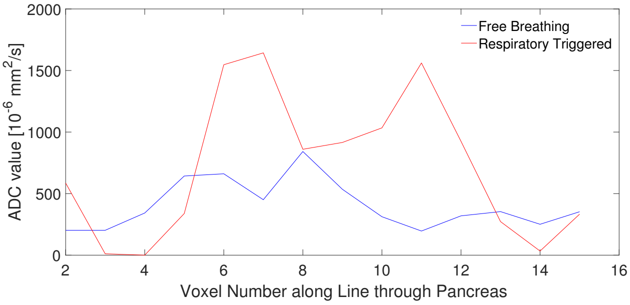

The plot of ADC$_{200,800}$ values along a line though the pancreas in the PE direction in patient 3.

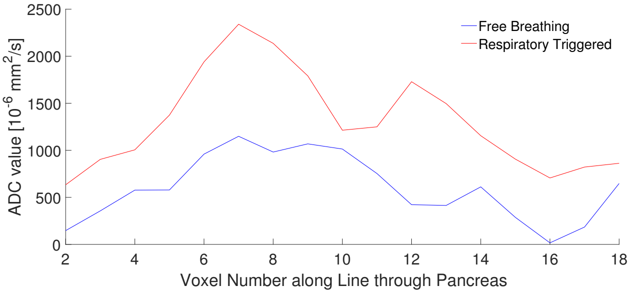

The plot of ADC$_{200,800}$ values along a line though the pancreas in the PE direction in patient 4.

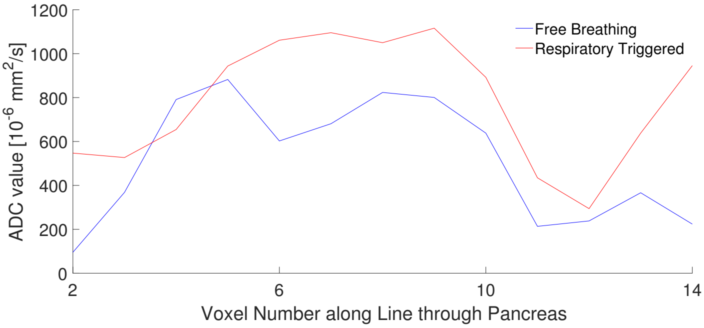

The plot of $\mathrm{ADC}_{200,800}$ values along a line though the pancreas in the PE direction in patient 5.

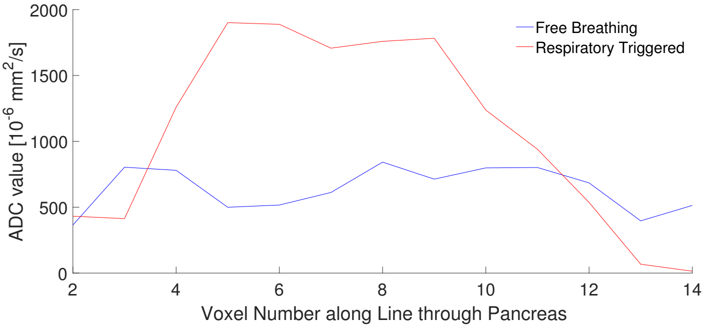

The plot of $\mathrm{ADC}_{200,800}$ values along a line though the pancreas in the PE direction in patient 6.

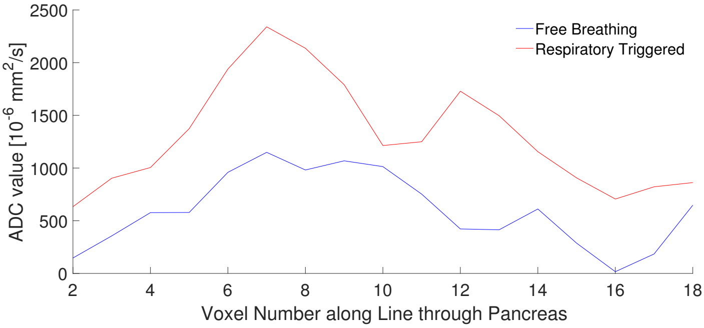

The plot of $\mathrm{ADC}_{200,800}$ values along a line though the pancreas in the PE direction in patient 7.

A.6 Plot of $\mathrm{ADC}_{0,200}$ along a Line through the Pancreas in read out Direction

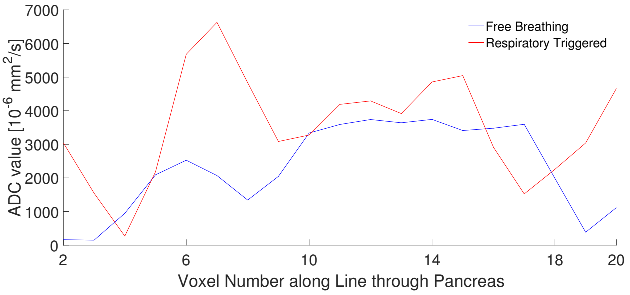

The plot of $\mathrm{ADC}_{0,200}$ values along a line though the pancreas in the RO direction in patient 1.

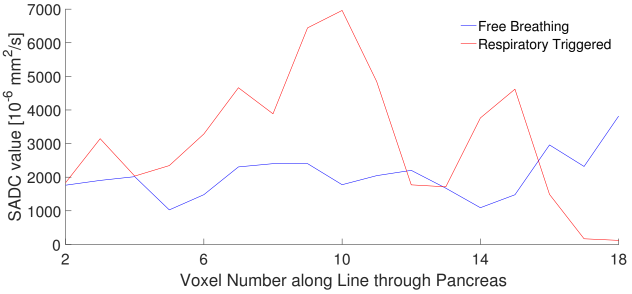

The plot of $\mathrm{ADC}_{0,200}$ values along a line though the pancreas in the RO direction in patient 3.

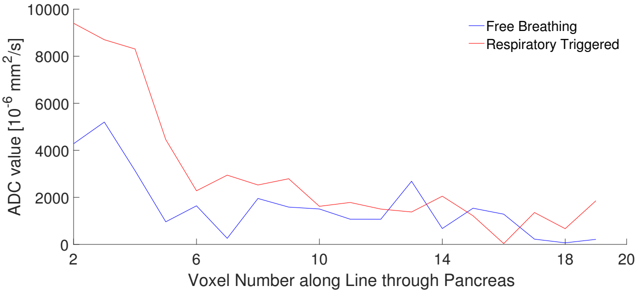

The plot of $\mathrm{ADC}_{0,200}$ values along a line though the pancreas in the RO direction in patient 4.

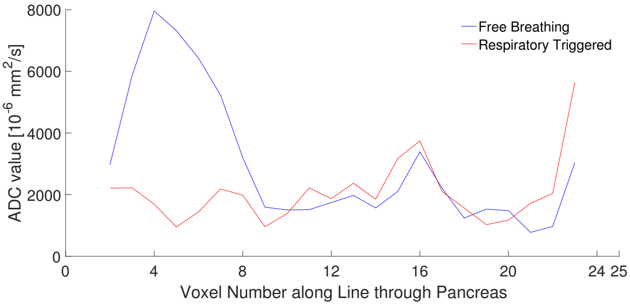

The plot of $\text{ADC}_{0,200}$ values along a line though the pancreas in the RO direction in patient 5.

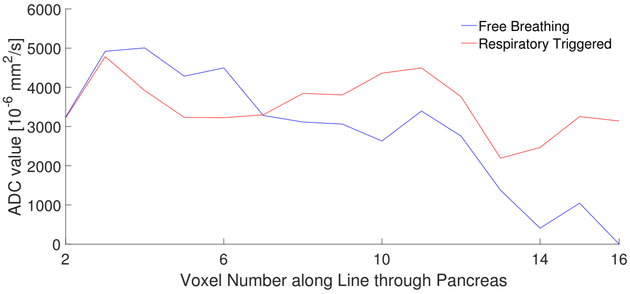

The plot of $\text{ADC}_{0,200}$ values along a line though the pancreas in the RO direction in patient 6.

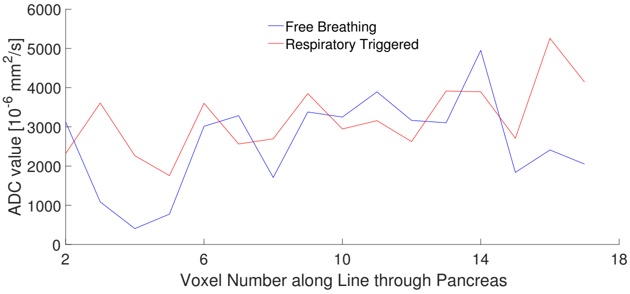

The plot of $\text{ADC}_{0,200}$ values along a line though the pancreas in the RO direction in patient 7.

A.7 Plot of $\mathrm{ADC}_{200,800}$ along a Line through the Pancreas in read out Direction

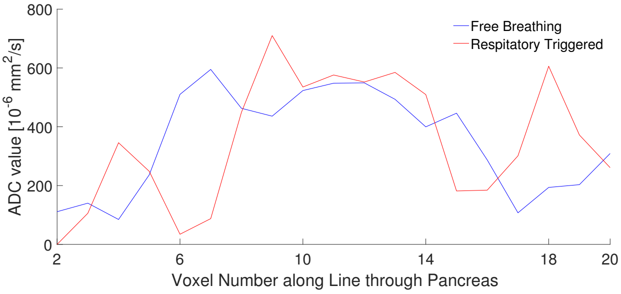

The plot of $\mathrm{ADC}_{200,800}$ values along a line though the pancreas in the RO direction in patient 1.

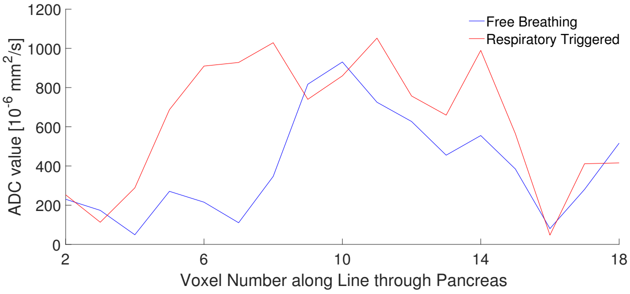

The plot of $\mathrm{ADC}_{200,800}$ values along a line though the pancreas in the RO direction in patient 3.

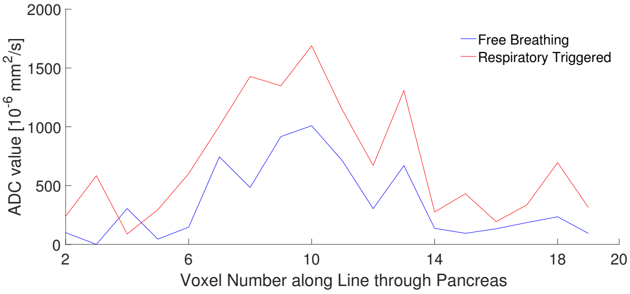

The plot of $\mathrm{ADC}_{200,800}$ values along a line though the pancreas in the RO direction in patient 4.

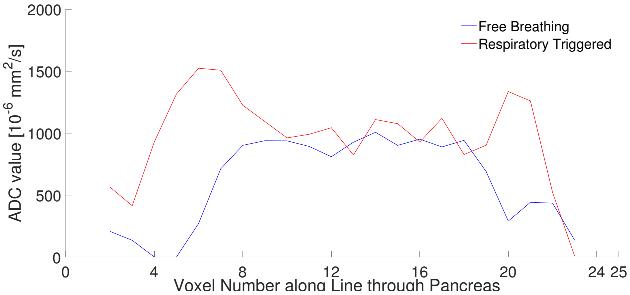

The plot of ADC$_{200,800}$ values along a line though the pancreas in the RO direction in patient 5.

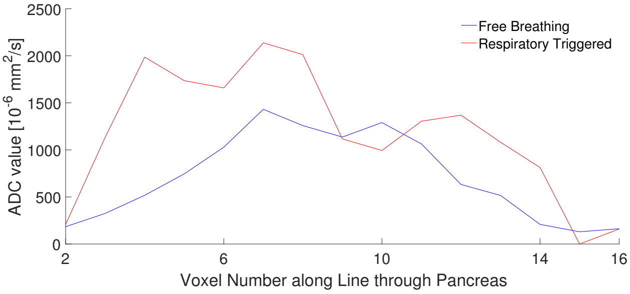

The plot of ADC$_{200,800}$ values along a line though the pancreas in the RO direction in patient 6.

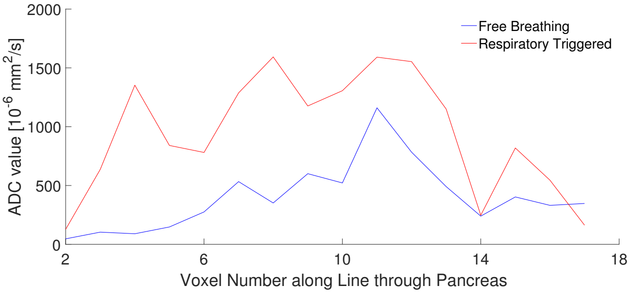

The plot of ADC$_{200,800}$ values along a line though the pancreas in the RO direction in patient 7.